Article

Cell

LXR/ApoE Activation Restricts Innate Immune Suppression in Cancer

Graphical Abstract

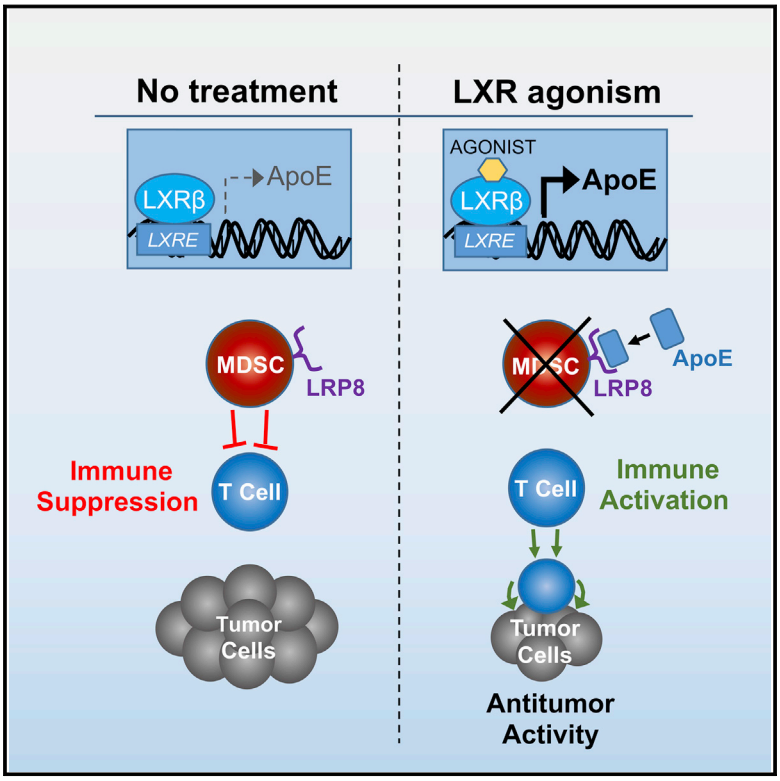

Highlights

- LXR agonism reduces immunosuppressive MDSC levels in mice and cancer patients
- LXR transcriptional target ApoE impairs MDSC survival
- LXR-induced MDSC depletion enhances activation of cytotoxic T lymphocytes (CTLs)
- CTL activation occurs in mice and patients, enhancing tumor immunotherapy in mice

Authors

Masoud F. Tavazoie, Ilana Pollack, Raissa Tanqueco, ..., Antoni Ribas, Daniel Mucida, Sohail F. Tavazoie

Correspondence

mtavazoie@mail.rockefeller.edu (M.F.T.), mucida@mail.rockefeller.edu (D.M.), stavazoie@mail.rockefeller.edu (S.F.T.)

In Brief

Therapeutic agonism of the LXR/ApoE axis promotes anti-tumor immunity by targeting immunosuppressive innate immune cells.

Tavazoie et al., 2018, Cell *172*, 1–16
February 8, 2018
https://doi.org/10.1016/j.cell.2017.12.026

CellPress

Please cite this article in press as: Tavazoie et al., LXR/ApoE Activation Restricts Innate Immune Suppression in Cancer, Cell (2018), https://doi.org/10.1016/j.cell.2017.12.026

Cell

LXR/ApoE Activation Restricts Innate Immune Suppression in Cancer

Masoud F. Tavazoie,[1,9,*] Ilana Pollack,[1,10] Raissa Tanqueco,[1,10] Benjamin N. Ostendorf,[1] Bernardo S. Reis,[2] Foster C. Gonsalves,[3] Isabel Kurth,[3] Celia Andreu-Agullo,[3] Mark L. Derbyshire,[1] Jessica Posada,[1] Shugaku Takeda,[3] Kimia N. Tafreshian,[1] Eric Rowinsky,[3] Michael Szarek,[3,8] Roger J. Waltzman,[3] Elizabeth A. Mcmillan,[1] Connie Zhao,[1] Monica Mita,[4] Alain Mita,[4] Bartosz Chmielowski,[5] Michael A. Postow,[6,7] Antoni Ribas,[5] Daniel Mucida,[2,*] and Sohail F. Tavazoie[1,11,*]

[1]Laboratory of Systems Cancer Biology, The Rockefeller University, New York, NY, USA
[2]Laboratory of Mucosal Immunology, The Rockefeller University, New York, NY, USA
[3]Rgenix, New York, NY, USA
[4]Cedars-Sinai Medical Center, Los Angeles, CA, USA
[5]Department of Medicine, University of California, Los Angeles, CA, USA
[6]Department of Medicine, Memorial Sloan Kettering Cancer Center, New York, NY, USA
[7]Weill Cornell Medical College, New York, NY, USA
[8]School of Public Health, Downstate Medical Center, Brooklyn, NY, USA
[9]Present address: Rgenix, New York, NY, USA
[10]These authors contributed equally
[11]Lead Contact
*Correspondence: mtavazoie@mail.rockefeller.edu (M.F.T.), mucida@mail.rockefeller.edu (D.M.), stavazoie@mail.rockefeller.edu (S.F.T.)
https://doi.org/10.1016/j.cell.2017.12.026

SUMMARY

Therapeutic harnessing of adaptive immunity via checkpoint inhibition has transformed the treatment of many cancers. Despite unprecedented long-term responses, most patients do not respond to these therapies. Immunotherapy non-responders often harbor high levels of circulating myeloid-derived suppressor cells (MDSCs)—an immunosuppressive innate cell population. Through genetic and pharmacological approaches, we uncovered a pathway governing MDSC abundance in multiple cancer types. Therapeutic liver-X nuclear receptor (LXR) agonism reduced MDSC abundance in murine models and in patients treated in a first-in-human dose escalation phase 1 trial. MDSC depletion was associated with activation of cytotoxic T lymphocyte (CTL) responses in mice and patients. The LXR transcriptional target ApoE mediated these effects in mice, where LXR/ApoE activation therapy elicited robust anti-tumor responses and also enhanced T cell activation during various immune-based therapies. We implicate the LXR/ApoE axis in the regulation of innate immune suppression and as a target for enhancing the efficacy of cancer immunotherapy in patients.

INTRODUCTION

Discoveries defining molecular checkpoints that constrain T cell activation represent a landmark in cancer treatment (Krummel and Allison, 1995; Okazaki and Honjo, 2007; Peggs et al., 2008). Overcoming such checkpoints through the use of therapeutic antibodies targeting the CTLA-4, PD-1, or PD-L1 cell surface receptors has been shown to be instrumental in promoting anti-tumor T cell responses in mice and in cancer patients (Hui et al., 2017; Iwai et al., 2005; Leach et al., 1996). Although the clinical responses to these therapies in multiple common cancer types can be remarkably prolonged, the majority of patients do not respond as a result of heightened immunosuppression in the tumor microenvironment or inadequate non-self-antigenic load within the tumor (Grzes et al., 2017; Sharma et al., 2017).

Myeloid-derived suppressor cells (MDSCs) are a heterogeneous population of suppressive innate immune cells that expand in the context of several disease states (Shipp et al., 2016; Youn et al., 2008). During malignancy, MDSC levels substantially increase in tumors and in the peripheral blood of patients harboring a broad array of malignancies, including melanoma and lung, breast, and ovarian cancers (Youn et al., 2008). MDSCs suppress both innate and adaptive immunity within the tumor microenvironment via production of various immune-suppressive molecules (Gabrilovich et al., 2012; Sinha et al., 2007). Consequently, patients with cancer who have high levels of circulating MDSCs have been found to respond poorly to checkpoint blockade (Meyer et al., 2014; Weber et al., 2016). Mirroring these human clinical findings, MDSC levels become elevated in multiple murine tumor models, where they mediate immunosuppression as well as angiogenesis (Gabrilovich et al., 2012). The signals, pathways, and biology that regulate MDSC formation, homeostasis, and function are areas of active investigation. There are currently no approved therapeutic agents that specifically target MDSCs.

Apolipoprotein E (ApoE) is a secreted protein implicated in lipoprotein metabolism as well as the pathogenesis of Alzheimer's disease and atherosclerosis (Tall and Yvan-Charvet, 2015). We recently revealed an additional role for ApoE in the pathogenesis of metastatic progression (Pencheva et al., 2012). We observed

Please cite this article in press as: Tavazoie et al., LXR/ApoE Activation Restricts Innate Immune Suppression in Cancer, Cell (2018), https://doi.org/10.1016/j.cell.2017.12.026

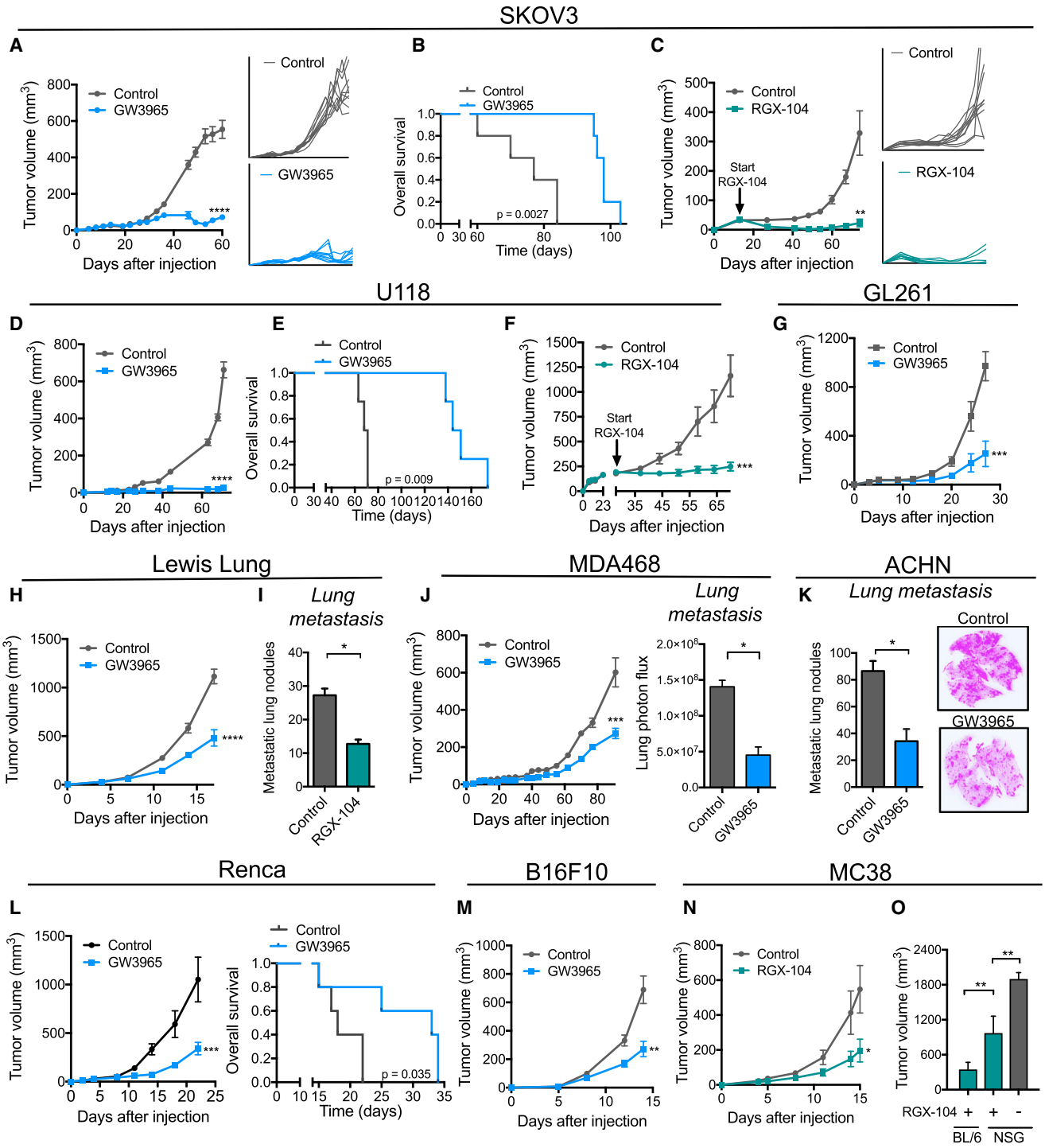

Figure 1. LXR Agonist Treatment Robustly Suppresses Tumor Growth and Progression across a Broad Set of Mouse and Human Tumors

(A–C) Tumor growth by 1 × 10^6 SKOV3 ovarian cancer cells subcutaneously injected into NOD SCID (A) or recombination-activating gene-deficient (*Rag*$^{-/-}$) (C) mice. Following tumor growth to 5–10 mm^3 (A) or 40–50 mm^3 (C) in volume, mice were fed control chow or chow supplemented with GW3965 (100 mg/kg/day) (A) or RGX-104 (100 mg/kg/day) (C); insets represent growth curves for individual tumors. (B) Survival of mice bearing the SKOV3 tumors shown in (A) (n ≥ 5). (D–F) Tumor growth by 1 × 10^6 U118 glioblastoma cells subcutaneously injected into NOD SCID mice. Following tumor growth to 5–10 mm^3 (D) or 200–250 mm^3 (F) in volume, mice were fed control chow or chow supplemented with GW3965 (100 mg/kg) (D) or RGX-104 (100 mg/kg) (F). (E) Survival of mice bearing the U118 tumors shown in (D) (n ≥ 5).

(legend continued on next page)

that ApoE impedes melanoma cell invasiveness and endothelial cell recruitment, two metastatic phenotypes, serving as a key barrier to metastatic colonization. Overexpression of multiple *Apoe*-targeting microRNAs in metastatic melanoma cells was found to silence this metastasis-suppressive protein and promote metastasis formation (Pencheva et al., 2012).

Liver-X receptors (LXRβ and LXRα) are members of the nuclear hormone receptor family of transcription factors that drive transcriptional activation of *Apoe* as well as other genes involved in cholesterol, fatty acid, and glucose metabolism (Apfel et al., 1994; Evans and Mangelsdorf, 2014; Hong and Tontonoz, 2014; Willy et al., 1995). Consistent with the ability of LXRs to drive ApoE systemic expression, pharmacological activation of the ubiquitously expressed *LXRβ* isoform was found to suppress melanoma tumor progression and metastatic colonization—effects caused by ApoE-mediated suppression of pro-metastatic invasion and endothelial recruitment phenotypes (Pencheva et al., 2014). Moreover, others have shown LXR agonism to inhibit tumorigenic phenotypes such as proliferation and survival (Lin and Gustafsson, 2015; Nelson et al., 2013; Villa et al., 2016). Interestingly, in our study of LXR effects on melanoma, LXR activation elicited more pronounced anti-tumor effects in genetically initiated immune-competent mice (Pencheva et al., 2014), suggesting potential immune-mediated consequences.

Such robust anti-tumor effects in melanoma motivated us to investigate the breadth of anti-tumor efficacy upon LXR agonism across a broad array of cancers as well as potential immune-dependent effects. Here we demonstrate a role for LXR and its transcriptional target *Apoe* in the regulation of MDSC abundance and, consequently, anti-tumor immunity.

RESULTS

LXR Activation Suppresses Tumor Growth and Reduces MDSC Abundance

We had previously observed that pharmacological activation of LXR using the LXRβ-selective agonist GW3965 suppressed melanoma angiogenesis, tumor growth, and metastatic colonization (Pencheva et al., 2014). LXRβ is a ubiquitously expressed nuclear receptor, and the anti-metastatic effects of LXRβ agonism were found to be mediated by both tumoral and host (stromal) tissue LXRβ activation (Pencheva et al., 2014). These observations motivated us to test the effect of LXRβ activation across a broad set of cancers arising from diverse tissues. Concomitantly, we tested a more potent LXRβ agonist, RGX-104 (Figure S1A), which is currently in a multicenter national phase 1 clinical trial in cancer patients (ClinicalTrials.Gov, NCT02922764). Oral administration of GW3965 or RGX-104 to animals bearing palpable tumors significantly suppressed the growth of multiple cancer types (Figures 1A–1O and S1B–S1F). Strong tumor growth suppression was also observed in animals bearing large tumors (Figures 1C and 1F). In some instances, LXRβ agonist treatment caused partial or complete tumor regression (Figures 1A and 1C). Responses were seen across a wide spectrum of malignancies, including lung cancer, melanoma, glioblastoma, and ovarian, renal cell, triple-negative breast, and colon cancer (Figures 1A–1O). Interestingly, strong anti-tumor therapeutic responses were observed in immunocompetent mice as well as in animals lacking adaptive immunity (Figures 1A and 1C). To determine whether LXRβ agonism mediates anti-tumor immunological effects, we compared the anti-tumor effects of LXRβ agonism on the growth of a syngeneic tumor (MC38) in a fully immunocompetent C57BL/6 model to an immunodeficient non-obese diabetic (NOD) severe combined immunodeficiency (SCID) gamma (NSG) model. LXRβ agonism significantly reduced MC38 tumor growth in fully immunocompetent mice (Figure 1N). MC38 tumors grew significantly larger during LXR therapy in immunodeficient mice relative to immunocompetent mice (Figure 1O), suggesting an immunological role for LXRβ agonism in tumor growth suppression. Furthermore, tumors grew significantly larger in NSG mice in the absence of LXRβ agonism than in treated NSG mice, consistent with previously established roles for LXRβ agonism in affecting tumorigenic phenotypes such as angiogenesis and invasiveness (Pencheva et al., 2014). These findings reveal that LXR activation elicits anti-tumor activity across a broad array of cancers and suggest that the anti-tumor effects of LXR activation are in part immunological in nature.

(G) Tumor growth by 2.5×10^5 GL261 glioblastoma cells subcutaneously injected into C57BL/6 mice. Following tumor growth to 5–10 mm^3 in volume, mice were fed control chow or chow supplemented with GW3965 (100 mg/kg) ($n \geq 5$).

(H and I) Tumor growth (H) and metastasis (I) by 2×10^5 LLC lung cancer cells subcutaneously injected into C57BL/6 mice. Following tumor growth to 5–10 mm^3 (H) or 30–40 mm^3 in volume (I), mice were fed control chow or chow supplemented with GW3965 (100 mg/kg) (H) or RGX-104 (100 mg/kg) (I). (I) Quantification of macroscopic metastatic nodules in H&E-stained lungs extracted on day 15 ($n \geq 5$).

(J) Tumor growth and bioluminescence quantification of lung metastasis of 1×10^6 MDA468 breast cancer cells subcutaneously injected into NOD SCID mice. Following tumor growth to 5–10 mm^3 in volume, mice were fed control chow or chow supplemented with GW3965 (100 mg/kg) ($n \geq 4$).

(K) Quantification and exemplary images of macroscopic metastatic nodules in H&E-stained lungs extracted 71 days after subcutaneous injection of 1×10^6 ACHN renal cancer cells; mice were fed control chow or chow supplemented with GW3965 (100 mg/kg) when tumors reached 5–10 mm^3 ($n \geq 4$).

(L) Tumor growth by 5×10^4 Renca renal cancer cells subcutaneously injected into syngeneic C57BL/6 mice. Following tumor growth to 5–10 mm^3 in volume, mice were fed control chow or chow supplemented with GW3965 (100 mg/kg). Survival of mice bearing Renca tumors is shown ($n \geq 5$).

(M) Tumor growth by 5×10^4 B16F10 cells subcutaneously injected into C57BL/6 mice. Following tumor growth to 5–10 mm^3 in volume, mice were fed control chow or chow supplemented with GW3965 (100 mg/kg) ($n \geq 5$).

(N) Tumor growth by 5×10^5 MC38 colon cancer cells subcutaneously injected into C57BL/6 mice. Following tumor growth to 5–10 mm^3 in volume, mice were fed control chow or chow supplemented with RGX-104 (100 mg/kg) ($n \geq 6$).

(O) Tumor volume on day 16 by 5×10^5 MC38 cells injected subcutaneously into C57BL/6 or NSG mice. Following tumor growth to 5–10 mm^3 in volume, mice were fed control chow or chow supplemented with RGX-104 (100 mg/kg) ($n \geq 6$).

Data represent mean ± SEM. See also Figure S1.

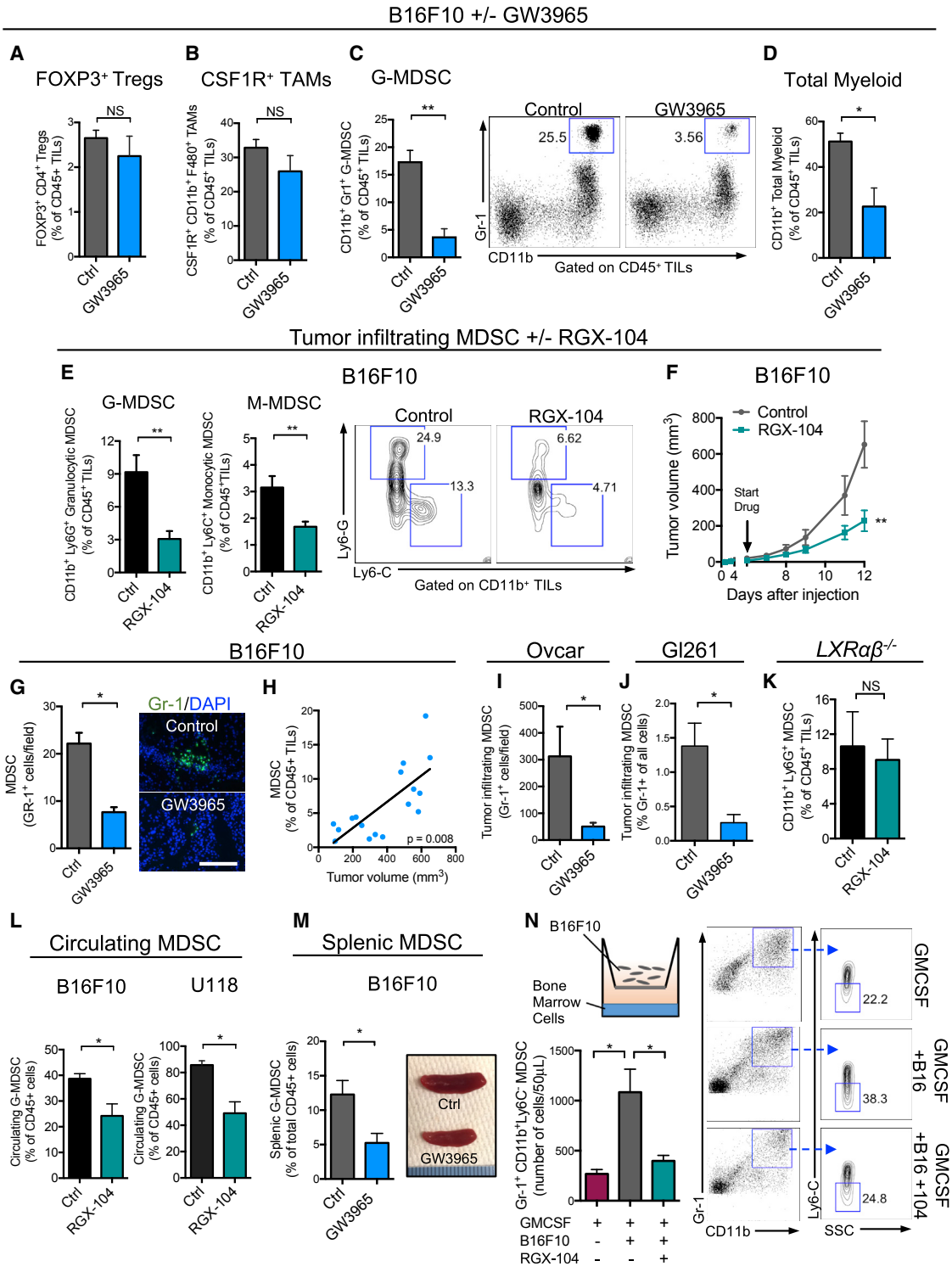

Figure 2. LXR Agonism Reduces Tumor-Infiltrating and Systemic Myeloid-Derived Suppressor Cells

(A–D) Percentage of tumor-infiltrating immune cells of total CD45$^+$ tumor-infiltrating leukocytes (TILs) in B16F10 tumors in mice treated with control or GW3965 (100 mg/kg) administered in chow when tumors reached 5–10 mm^3 in volume. Flow cytometry analysis was performed 14 days after tumor injection (n = 6). Shown are (A) Foxp3+ T regulatory cells, (B) CSF-1R+ tumor-associated macrophages, (C) total granulocytic myeloid-derived suppressor cells, and (D) total myeloid lineage cells. Representative plots show CD11b$^+$ Gr-1^{high} G-MDSC populations.

(legend continued on next page)

We hypothesized that LXR therapy may influence anti-tumor immunity by affecting an immunosuppressive cell population in the tumor microenvironment. To explore this, we performed flow cytometry analysis of B16F10 melanoma tumors derived from mice treated with or without the LXR agonist. We did not observe significant changes in the frequency of regulatory T cells (Tregs) or tumor-associated macrophages (TAMs)—two major immunosuppressive cell populations (Figures 2A and 2B). However, LXR agonism significantly reduced the abundance of tumoral granulocytic MDSCs (Figure 2C). In mice, MDSCs are comprised of $CD11b^{+}Gr1^{hi}$ ($Ly6C^{low}Ly6G^{high}$) granulocytic MDSCs (G-MDSCs, also referred to as polymorphonuclear [PMN]-MDSC) and $CD11b^{+}Gr1^{int}$ ($Ly6C^{high}Ly6G^{low}$) monocytic MDSC (M-MDSCs). Flow cytometry analysis revealed that LXR activation reduced both granulocytic (66% reduction) and monocytic (47% reduction) intra-tumoral MDSC subpopulations (Figures 2E and 2F). Immunofluorescence analysis of tumor sections confirmed a significant reduction in G-MDSCs (Figure 2G). We also observed a positive correlation between the percentage of tumor-infiltrating MDSCs and tumor volume (Figure 2H). We extended these observations to multiple additional models that responded robustly to LXR agonism, including human ovarian (Ovcar; Figure 2I), murine glioblastoma (GL261; Figure 2J), and lung cancer (Lewis lung carcinoma [LLC]; Figure S2A). Additionally, the effects of LXR activation on MDSCs were observed not only in the tumor microenvironment but in the circulation and spleen as well (Figures 2L and 2M). Finally, B16F10 tumors grown in mice that were deficient for both *LXRα* and *LXRβ* ($LXR\alpha\beta^{-/-}$ mice) failed to exhibit significant MDSC depletion (Figure 2K) or tumor growth inhibition (Figure S2B) upon LXR agonism, confirming that these pharmacologic effects are mediated by LXR activation. MDSCs can be expanded in the presence of granulocyte-macrophage colony-stimulating factor (GM-CSF) *in vitro* by culturing bone marrow cells in the basal chamber of a transwell and B16F10 melanoma cells in the apical chamber. Addition of an LXR agonist significantly reduced G-MDSC abundance in this system to a level comparable with omission of cancer cells (Figure 2N). These findings demonstrate that LXR activation reduces the abundance of tumoral MDSCs both *in vitro* and *in vivo*.

LXR-Mediated MDSC Depletion Reverses Tumor Immune Evasion

We next determined whether MDSC depletion caused by LXR activation affected adaptive immunity. Consistent with their established immune-suppressive nature, systemic MDSCs isolated from spleens of mice bearing B16F10 tumors suppressed $CD8^{+}$ T cell activation, as assessed by interferon γ (IFN-γ) production, and proliferation, as assessed by dilution of violet proliferation (brilliant violet [BV]) dye (Figure 3A). Moreover, MDSCs derived from LXR agonist-treated mice were less effective at suppressing T cell activation *in vitro* (Figure 3A), suggesting that LXR activation may affect MDSC survival and, potentially, suppressive function. Indeed, the tumor-infiltrating MDSC population remaining after LXR agonist treatment *in vivo* expressed higher levels of major histocompatibility complex (MHC) class II, consistent with a less immunosuppressive phenotype (Figures S3A and S3B; Almand et al., 2001).

MDSCs are known to suppress T cell activation. Consistent with this, LXR-mediated MDSC depletion was associated with an ~7-fold increase in the frequency of IFN-γ and Granzyme B double-positive tumor-infiltrating cytotoxic T lymphocytes (CTLs) (Figure 3B) *in vivo*. Importantly, *in vitro* LXR treatment of T cells in isolation did not directly modulate T cell activation or proliferation (Figure S3C), consistent with the MDSC dependence of these findings. Increased numbers of $PD\text{-}1^{+}$ $CD8^{+}$ CTLs have been observed to occur upon checkpoint inhibition in the B16 melanoma model (Curran et al., 2010), whereas their abundance in human melanoma tumors prior to therapy has been associated with increased responsiveness to immunotherapy (Tumeh et al., 2014). Moreover, $PD\text{-}1^{+}$ $CD8^{+}$ CTLs have been shown to represent the tumor antigen-recognizing and tumor-reactive T cell population in human patients (Gros et al., 2014). We observed an increased abundance of tumor-infiltrating $PD\text{-}1^{+}$ $CD8^{+}$ CTLs upon LXR agonist therapy (Figure 3C), consistent with a reversal of immune evasion after MDSC depletion. Furthermore, tumoral MDSC abundance negatively correlated with tumoral CTL activation (Figure 3D). Finally, although the abundance of these cells is low compared with CTLs, we observed an ~4-fold increase in the number of tumor-infiltrating IFN-γ^{+} tumor necrosis factor alpha (TNF-α^{+})

(E) Percent granulocytic (left) and monocytic (right) MDSCs of $CD45^{+}$ TILs in B16F10 tumors grown in mice treated with control or RGX-104 (80 mg/kg) administered intraperitoneally (i.p.) when tumors reached 5–10 mm^3. Flow cytometry analysis was performed 13 days after tumor injection ($n \geq 8$). Representative contour plots show $Ly6G^{+}$ granulocytic and $Ly6C^{+}$ monocytic populations.

(F) Mean tumor volume of the subcutaneous B16F10 tumors described in (E) ($n \geq 5$).

(G) Quantification of tumor-infiltrating $Gr\text{-}1^{+}$ cells in B16F10 tumors removed on day 11 after treatment with the control or GW3965 (100 mg/kg). Shown are representative images of $Gr\text{-}1^{+}$ immunofluorescence in B16F10 tumor sections after treatment with the control (top) or GW3965 (bottom). Five sections were imaged per tumor to achieve an average number of tumor-infiltrating $Gr\text{-}1^{+}$ cells per high-power field (n = 6). Scale bar, 143 μm.

(H) Correlation between the percentage of tumor-infiltrating G-MDSCs and tumor volume (n = 17).

(I and J) Quantification of tumor-infiltrating $Gr\text{-}1^{+}$ cells in Ovcar (I) and GL261 (J) tumors removed on days 81 (I) and 27 (J) after treatment with the control or GW3965 (100 mg/kg). Five sections were imaged per tumor to achieve an average number of tumor-infiltrating $Gr\text{-}1^{+}$ cells (n = 5).

(K) Percentage of G-MDSCs of total $CD45^{+}$ TILs in B16F10 tumors grown in $LXR\alpha\beta^{-/-}$ mice treated with the control or RGX-104 (100 mg/kg) when tumors reached 5–10 mm^3 ($n \geq 6$).

(L) Percentage of circulating G-MDSCs of total $CD45^{+}$ leukocytes in the peripheral blood of B16F10 (left) or U118 (right) tumor-bearing mice treated with the control or RGX-104 (100 mg/kg) (n = 5).

(M) Percentage of G-MDSCs of total $CD45^{+}$ splenocytes (n = 5). Shown are representative spleens of control or GW3965-treated mice after 10 days of treatment (right).

(N) Transwell MDSC differentiation assay. Bone marrow cells were cultured with B16F10 melanoma cells and GM-CSF for 6 days. On day 3, RGX-104 (2 μM) was added to the culture. The mean number of $Gr\text{-}1^{high}$ $CD11b^{+}$ cells per 50 μL of culture solution is shown, as assessed by flow cytometry on day 6.

Data represent mean ± SEM. See also Figure S2.

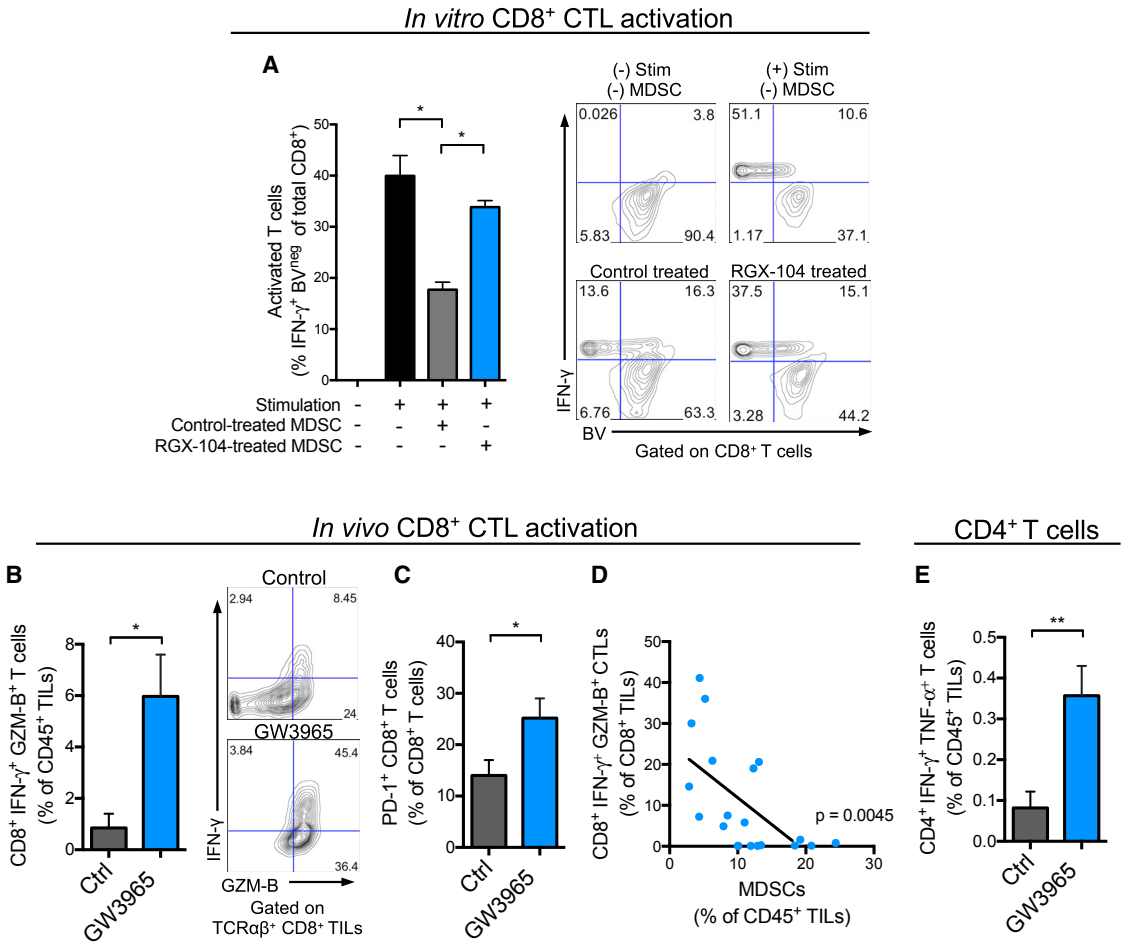

Figure 3. LXR Agonism Increases Tumor-Infiltrating Activated CD8$^+$ and CD4$^+$ T Cells

(A) Suppressive properties of splenic MDSCs isolated from tumor-bearing mice treated *in vivo* with control or RGX-104 (100 mg/kg) chow for 48 hr, as assessed by CD8$^+$ T cell activation (IFN-γ expression) and proliferation (BV dilution) after co-culture *in vitro*. Representative contour plots show IFN-γ expression and BV fluorescence of CD8$^+$ cells (n = 4).

(B) Percentage of IFN-γ- and Granzyme B (GZM-B)-expressing, activated CD8$^+$ T cells of total CD45$^+$ TILs from B16F10 tumors of control or GW3965-treated mice (100 mg/kg) after 10 days of treatment (n = 6). Representative contour plots show percentages of double-positive cells.

(C) Percentage of PD-1$^+$ CD8$^+$ T cells of total tumor-infiltrating CD8$^+$ T cells from B16F10 tumors of control or GW3965-treated mice (100 mg/kg, 10 days) (n = 6).

(D) Correlation between tumor-infiltrating CD8$^+$IFN-γ$^+$GZM-B$^+$ T cells and G-MDSCs, reported as percentages of total CD8$^+$ and CD45$^+$ TILs, respectively (n = 20).

(E) Percentage CD4$^+$IFN-γ$^+$TNF-α$^+$ T cells of total CD45$^+$ TILs from B16F10 tumors treated for 10 days with the control or GW3965 (100 mg/kg) (n = 6).

Data represent mean ± SEM. See also Figure S3.

double-positive CD4$^+$ T cells upon LXRβ-mediated MDSC depletion (Figure 3E). Together, the above findings reveal that *bona fide* MDSCs are targeted by LXR therapy, which results in activation of CTLs and a Th1 anti-tumor immune phenotype.

To determine whether LXR agonist therapy elicits a tumor antigen-specific T cell response in a polyclonal system, we performed MHC class I-gp100 antigen tetramer staining in control and LXR agonist-treated mice bearing B16F10 tumors that endogenously express the gp100 (Pmel) antigen. We observed a significant expansion of activated tumor-infiltrating gp100-specific CD8$^+$ T cells upon LXR agonism that mirrored the total CD8$^+$ T cell activation response (Figures S3D–S3H). Activated tumor antigen-selective T cells expressed higher levels of both CD69 and PD-1 (Figure S3F).

LXR Activation Targets MDSCs by Reducing Their Survival

LXR activation could reduce MDSC abundance by repressing MDSC generation. Alternatively, LXR activation could affect MDSC maintenance—by increasing cell death, for example. To distinguish between these possibilities, we analyzed the effect of LXR therapy on MDSC abundance within the bone marrow. LXR activation did not significantly alter the abundance (Figure 4A) or expression of apoptotic markers (Figure 4B) on bone marrow MDSCs. The lack of apparent LXR-mediated effects on

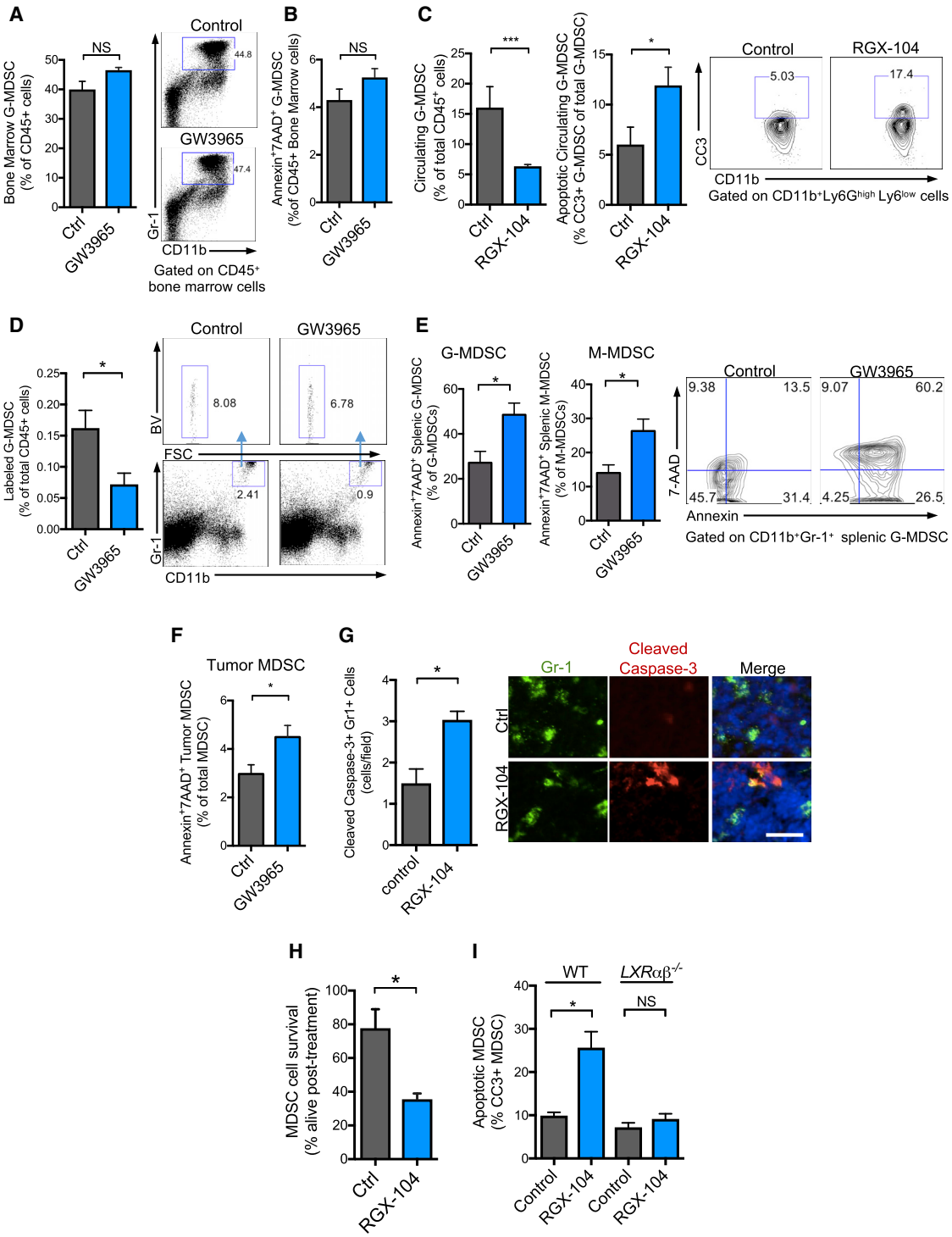

Figure 4. LXR Agonist Treatment Promotes MDSC Apoptosis *In Vivo* and *In Vitro*

(A) Percentage of Gr1$^+$ CD11b$^+$ G-MDSCs of total CD45$^+$ leukocytes in the bone marrow of GW3965-treated (100 mg/kg) mice compared with controls after 10 days of treatment (n = 5).

(B) Percentage of Annexin$^+$ 7AAD$^+$ G-MDSCs of total CD45$^+$ bone marrow cells after GW3965 treatment (100 mg/kg) for 10 days compared with controls (n = 5).

(C) Percentage of circulating G-MDSCs of total CD45$^+$ leukocytes in RGX-104-treated (100 mg/kg) mice compared with controls after 8 days of treatment (left) and percentage of cleaved caspase-3$^+$ (CC3+) G-MDSCs of total circulating G-MDSCs from B16F10 tumor-bearing mice treated for 8 days with either the control or RGX-104 (100 m/kg) (right) (n = 8). Contour plots show the population of cleaved caspase-3$^+$ MDSCs.

(legend continued on next page)

bone marrow MDSC levels suggests that LXR therapy may promote MDSC elimination peripherally. Consistent with this, LXR agonist treatment significantly increased apoptosis of MDSCs in the peripheral blood of mice, as assessed by cleaved caspase-3 staining (Figure 4C). To further confirm that LXR treatment affects MDSC fate, MDSCs were isolated from spleens of tumor-bearing mice, labeled, and adoptively transferred into non-tumor-bearing recipient mice, which subsequently received either an LXR agonist or vehicle control for 48 hr. Flow cytometry analysis of spleens from recipient mice demonstrated a significant (56%) reduction in transferred MDSCs (Figure 4D). Similar studies in tumor-bearing recipient mice revealed that LXR agonism for a short duration (36 hr) was sufficient to increase the population of total transferred MDSCs undergoing apoptosis (Figure S4A). These findings suggest that enhanced cell death or active killing is the predominant mechanism of MDSC reduction. LXR activation also depleted the corresponding $CD11b^{+}Gr1^{+}$ myeloid population in non-tumor-bearing mice (Figures S4B and S4C), which represent a small fraction (~1%–2%) of leukocytes in the spleen that possess some immunosuppressive capacity (Figure S4D), albeit to a lesser extent than activated MDSCs. Consistent with an apoptosis-mediated mechanism, LXR therapy of tumor-bearing mice significantly increased the fraction of MDSCs staining positive for Annexin and 7-amino-actinmycin D (7AAD) both in spleens and in tumors (Figures 4E and 4F). Immunofluorescence for cleaved caspase-3 supported these observations (Figure 4G). Although we cannot exclude the possibility that LXR activation affects MDSC abundance through other means, such as active killing, these findings suggest that enhanced apoptosis contributes to LXR-dependent MDSC depletion.

We next investigated whether LXR agonism could act directly on MDSCs to impair survival. *In vitro* LXR agonist treatment of MDSCs obtained from tumor-bearing mice significantly reduced cell survival (Figure 4H). LXR agonism *in vitro* significantly enhanced MDSC cleaved caspase-3 staining (Figure 4I), consistent with enhanced apoptosis. Importantly, this effect was abolished in MDSCs obtained from $LXR\alpha\beta^{-/-}$ mice (Figure 4I). No effect on apoptosis was observed with LXR agonist treatment of MDSCs isolated from bone marrow of tumor-bearing mice (Figure S4E), consistent with *in vivo* observations. We did not observe a significant effect on MDSC proliferation, as assessed by Ki-67 staining, and only a small effect on MDSC cell adhesion, which was of unclear physiological significance (Figures S4F and S4G). These observations suggest that LXR activation promotes MDSC elimination by repressing MDSC survival.

Genetic Evidence of a Role for the LXR/ApoE Axis in MDSC Survival and Tumor Growth

Liver-X receptors transcriptionally activate a suite of genes involved in reverse cholesterol transport. We have shown previously that the anti-tumor effects of LXR agonists were mediated by the ubiquitously expressed LXRβ nuclear hormone receptor and its transcriptional target *Apoe* (Pencheva et al., 2014). The anti-tumor effects of LXR agonism have been shown previously to be mediated by *ApoE* induction in both the tumoral and host (non-tumoral) compartments (Pencheva et al., 2014). A variety of cell types, such as macrophages, hepatocytes, adipocytes, and endothelial cells, produce ApoE, which is secreted and circulates systemically within lipoprotein particles. To investigate the role of ApoE in LXR-mediated MDSC depletion, we tested the effect of LXR therapy on tumoral MDSC abundance in the context of *Apoe* genetic inactivation in the stroma and systemically as well as ApoE depletion in tumor cells. In contrast to wild-type mice, LXR treatment failed to significantly reduce tumoral MDSC levels or tumor volume in $Apoe^{-/-}$ mice bearing ApoE-depleted B16F10 tumor cells (Figures 5A and 5B). Additionally, adoptive transfer of $Apoe^{-/-}$ MDSCs to $Apoe^{-/-}$ mice did not result in depletion of adoptively transferred MDSCs *in vivo* upon LXR treatment (Figure 5C). Similar observations were made *in vitro*, where $Apoe^{-/-}$ MDSCs were found to be resistant to LXR-mediated effects on survival (Figures S5A and S5B). Similar to our observations in the B16F10 melanoma model, *Apoe*-deficient mice bearing ApoE-depleted GL261 (glioblastoma) and LLC (lung) tumors failed to respond to LXR therapy, contrasting our findings made in wild-type mice (Figures S5C and S5D). These findings reveal that the LXR transcriptional target gene *Apoe* mediates LXR-dependent MDSC depletion.

To investigate whether ApoE could represent a physiological regulator of $CD11b^{+}Gr1^{+}$ myeloid cell maintenance in the absence of malignancy, we compared the levels of these cells in ApoE-deficient mice relative to wild-type mice. ApoE-deficient mice harbored significantly higher levels of both $CD11b^{+}Gr1^{high}$ (granulocytic) and $CD11b^{+}Gr1^{int}$ (monocytic) myeloid cells *in vivo* relative to wild-type counterparts (Figure 5D). We found that $Apoe^{-/-}$ myeloid cells functionally suppressed T cells in co-culture T cell assays (Figure S5E), confirming that MDSCs expanded in the setting of ApoE deficiency possess immunosuppressive activity.

We next investigated the effect of ApoE deficiency on tumor growth. Melanoma and glioblastoma tumors exhibited accelerated tumor growth in ApoE-deficient mice (Figure 5F). Higher

(D) Percentage of labeled, adoptively transferred G-MDSCs of total $CD45^{+}$ splenocytes from recipient mice treated for 48 hr with GW3965 or control after adoptive transfer. Representative plots show labeled $CD11b^{+}Gr\text{-}1^{+}$ MDSCs from control and GW3965-treated recipient mice (n = 5).

(E) $Annexin^{+}$ $7AAD^{+}$ granulocytic (left) and monocytic (right) $CD11b^{+}Gr\text{-}1^{+}$ MDSCs of total $CD45^{+}$ splenic leukocytes. Representative contour plots show double-positive cells gated on $CD11b^{+}$ $Gr1^{high}$ G-MDSCs (n = 5).

(F) Percent $Annexin^{+}$ $7AAD^{+}$ G-MDSCs of total $CD11b^{+}$ $Gr1^{+}$ G-MDSCs in B16F10 tumors (n = 5).

(G) Quantification of caspase-3^{+} $Gr\text{-}1^{+}$ cells in the spleens of B16F10 tumor-bearing mice after 12 days of control or RGX-104 (100 mg/kg) treatment. 5 sections per spleen were imaged to calculate an average number of double-positive cells per high-power field (n = 5). Shown are representative immunofluorescence images of splenic sections stained for Gr-1 and cleaved caspase-3 treated with the control (top) or RGX-104 (100 mg/kg) (bottom). Scale bar, 29 μm.

(H) Percentage of $CD11b^{+}Gr\text{-}1^{+}$ MDSCs alive after 3 hr of treatment *in vitro* with RGX-104 (2 μM). MDSCs were isolated from B16F10 tumor-bearing mice (n = 4).

(I) Percentage of cleaved caspase-3^{+} $Gr1^{+}$ $CD11b^{+}$ MDSCs from wild-type (WT) or $LXR\alpha\beta^{-/-}$ B16F10 tumor-bearing mice treated *in vitro* with 1 μM RGX-104 or vehicle control after a 6-hr culture (n = 4).

Data represent mean ± SEM. See also Figure S4.

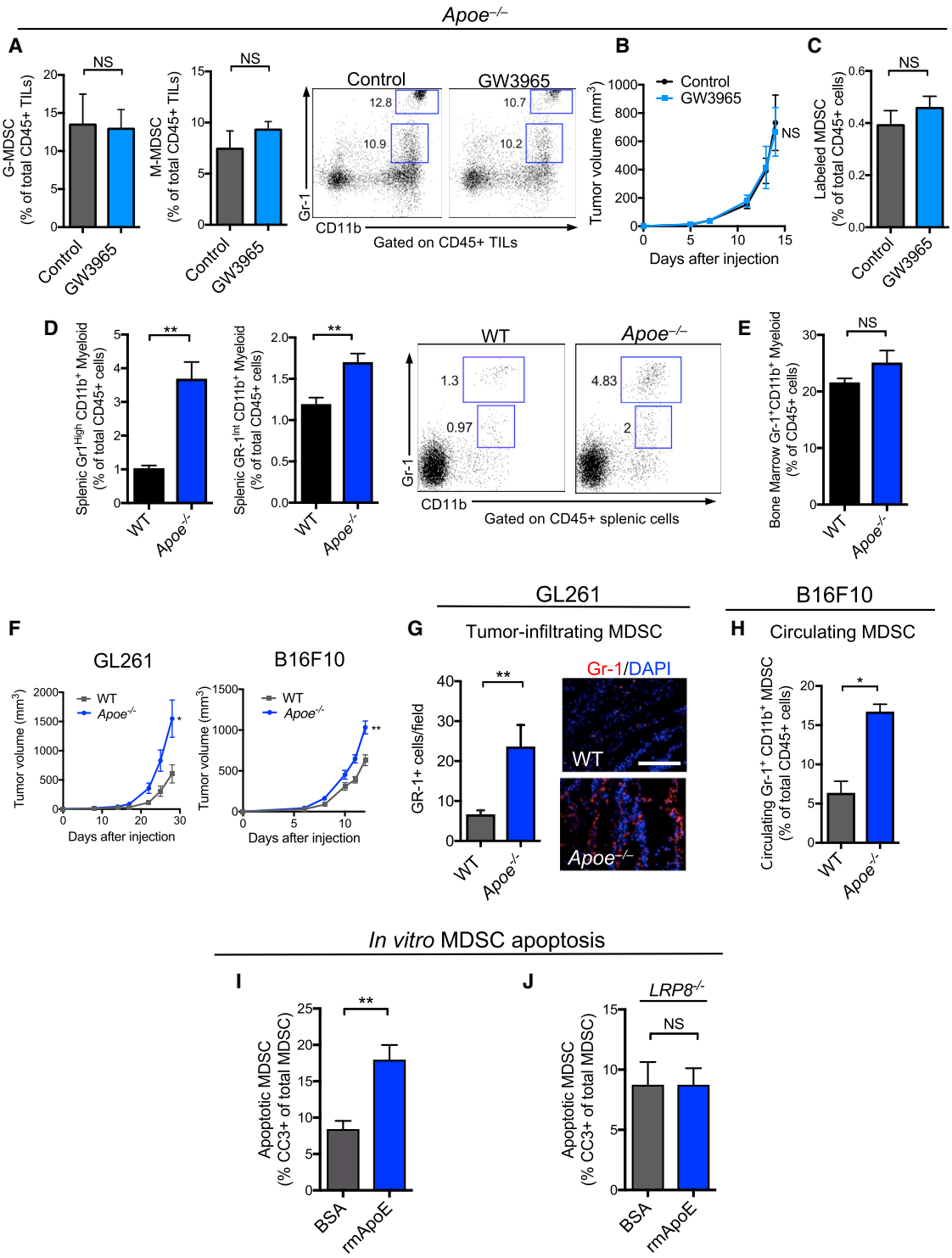

Figure 5. ApoE/LRP8 Signaling Regulates MDSC Survival Downstream of LXR Agonism

(A) Percentage of tumor-infiltrating granulocytic (left) and monocytic (right) MDSCs of total CD45$^+$ tumor-infiltrating leukocytes in B16F10 tumors in *Apoe*$^{-/-}$ mice treated with the control or GW3965 (100 mg/kg) (n $\geq$ 4). Representative plots show CD11b$^+$Gr1^{high} granulocytic and CD11b$^+$Gr1^{int} monocytic populations.

(B) Mean tumor growth of control or GW3956-treated ApoE-depleted B16F10 tumors injected into *Apoe*$^{-/-}$ mice (n = 4).

(C) Percentage of labeled, adoptively transferred, ApoE-deficient (*Apoe*$^{-/-}$) MDSCs of total CD45$^+$ splenocytes from *ApoE*$^{-/-}$ recipient mice treated for 48 hr with GW3965 or the control after adoptive transfer (n = 5).

(D) Percentage of splenic granulocytic (left) and monocytic (right) CD11b$^+$Gr-1$^+$ myeloid cells of total CD45$^+$ splenic leukocytes in WT and *Apoe*$^{-/-}$ mice (n = 5).

(legend continued on next page)

levels of circulating and intratumoral MDSCs were observed in these ApoE-deficient tumor-bearing mice, as assessed by immunofluorescence (Figure 5G) and flow cytometry (Figure 5H). Finally, we determined whether ApoE protein was sufficient to impair MDSC survival. *In vitro* treatment of MDSCs with recombinant ApoE protein significantly enhanced MDSC apoptosis, as assessed by MDSC cleaved caspase-3 staining (Figure 5I). Interestingly, in contrast to LXR treatment, ApoE treatment was capable of inducing apoptosis of MDSCs isolated from the bone marrow of tumor-bearing mice (Figure S5G), suggesting that bone marrow MDSCs are sensitive to ApoE but resistant to LXR agonist treatment, possibly because of reduced LXR expression detected in this compartment (serial analysis of gene expression [SAGE] profile). Last, we observed enhanced survival of *Apoe*$^{-/-}$ MDSCs compared with wild-type MDSCs *in vitro* in the absence of LXR treatment (Figure S5F). These findings uncover ApoE as a suppressor of MDSC survival and reveal that ApoE mediates the effects of LXRβ agonism on MDSC depletion.

LXR/ApoE Signaling Suppresses MDSC Survival via the LRP8 Receptor

We had observed previously that ApoE mediates its effects on endothelial migration via the LRP8 ApoE receptor (Pencheva et al., 2012). We hypothesized that LRP8 may also mediate ApoE-dependent MDSC effects. To test this, we treated *LRP8*$^{-/-}$ (Dieckmann et al., 2010) or wild-type MDSCs with recombinant ApoE protein. Although ApoE significantly enhanced apoptosis of wild-type MDSCs, it failed to significantly augment apoptosis of *LRP8*$^{-/-}$ MDSCs (Figure 5J). Consistent with these findings, LXR agonism did not significantly increase MDSC apoptosis in *LRP8*$^{-/-}$ tumor-bearing mice (Figures S5H and S5I). These findings reveal that LXR activation causes the LXR target gene ApoE to repress MDSC survival via its action on LRP8 receptors.

LXR Activation Augments Anti-tumor Responses in Immunotherapy Models

Adoptive T cell and engineered chimeric antigen receptor (CAR) therapies have provided significant clinical benefits in subsets of cancer patients (Davila and Brentjens, 2016; Lim and June, 2017). These approaches, however, are hindered by the immunosuppressive microenvironment of solid tumors (Wrzesinski et al., 2010). We thus investigated the effect of LXR activation therapy on anti-tumor responses in the presence of tumor antigen-specific T cells using a mouse model of adoptive T cell therapy. Consistent with previous observations (Overwijk et al., 1998), adoptive transfer of CTLs bearing transgenic T cell receptors specific for the melanoma tumor antigen gp100 (Pmel) into vaccinated mice bearing B16F10 tumors yielded some anti-tumor activity (Figures 6A and 6B). However, we observed a substantial increase in CTL anti-tumor activity upon co-administration of an LXR agonist, as assessed by reduced tumor volume and increased mouse survival (Figures 6A and 6B). This enhancement of anti-tumor activity was elicited in the absence of a preconditioning regimen, suggesting that the reversal of immune evasion with LXR therapy alone was of sufficient magnitude to enhance the anti-tumor activity of transferred CTLs.

To investigate whether LXR therapy could augment checkpoint blockade in the presence of a large number of primed antigen-specific T cells, RGX-104 was combined with both anti-PD-1 therapy and adoptive T cell therapy with tumor-antigen (gp100)-specific CD8$^+$ T cells in vaccinated mice. In this adoptive cell therapy paradigm, co-administration of RGX-104 with anti-PD-1 was superior to administration of either RGX-104 or anti-PD-1 alone (Figure 6C). Moreover, this triple combination therapy resulted in substantial anti-tumor activity and was well tolerated, demonstrating the potential for LXR agonists to enhance anti-tumor immunity even in the presence of immune priming and checkpoint blockade. We next investigated the potential for LXR activation therapy to enhance checkpoint blockade in an aggressive syngeneic model of lung cancer progression. Co-administration of RGX-104 and anti-PD-1 therapy in the Lewis lung cancer model yielded synergistic anti-tumor activity in the absence of adjuvant tumor antigen vaccination (Figure 6D). Importantly, co-administration of RGX-104 with anti-PD-1 therapy was well tolerated by mice, with no overt signs of toxicity.

Anti-PD-1 or anti-CTLA-4 checkpoint inhibition in the B16F10 murine melanoma model was reported to yield limited anti-tumor activity in the absence of adjuvant therapy (Curran and Allison, 2009). Co-administration of RGX-104 to anti-PD-1 significantly enhanced anti-tumor activity compared with single-agent anti-PD1 therapy in the absence of adjuvant therapy or vaccination (Figure 6E). Such combined RGX-104/anti-PD-1 therapy significantly augmented tumor-infiltrating cytotoxic T cell abundance relative to anti-PD-1 therapy alone (Figure 6F). Finally, we investigated the efficacy of LXR therapy in a model in which augmented tumoral MDSC accumulation is known to impair checkpoint efficacy. Consistent with published reports, frequent administration of Gvax (irradiated B16 melanoma cells engineered to overexpress GM-CSF) significantly increased the number of tumor-infiltrating MDSCs (Figure 6G). Anti-PD-1 therapy was ineffective at reducing tumor growth in the presence of this Gvax regimen, wherein tumoral MDSCs were

(E) Percentage of CD11b$^+$Gr-1$^+$ myeloid cells of total CD45$^+$ leukocytes in the bone marrow of WT and *Apoe*$^{-/-}$ mice (n = 5).
(F) Mean tumor growth of GL261 (left) and B16F10 (right) grown in WT and *Apoe*$^{-/-}$ mice (n = 5).
(G) Quantification (left) and representative immunofluorescence staining (right) of tumor-infiltrating Gr-1$^+$ cells in GL261 tumors grown in WT and *Apoe*$^{-/-}$ mice for 27 days (n = 6). 5 sections per tumor were imaged to calculate an average number of Gr-1$^+$ cells per high-power field (n = 5). Scale bar, 143 μm.
(H) Percentage of circulating Gr-1$^+$ CD11b$^+$ G-MDSCs of total CD45$^+$ cells after 7 days of tumor growth in WT or *Apoe*$^{-/-}$ mice (n = 5).
(I) Percentage of cleaved caspase-3$^+$ (CC3+) Gr1$^+$ CD11b$^+$ splenic MDSCs from WT B16F10 tumor-bearing mice treated *in vitro* with 5 μM BSA or recombinant mouse ApoE protein (rmApoE) after 6-hr culture (n = 4).
(J) Percentage of cleaved caspase-3$^+$ (CC3+) Gr1$^+$ CD11b$^+$ splenic MDSCs from *LRP8*$^{-/-}$ B16F10 tumor-bearing mice treated *in vitro* with 5 μM BSA or rmApoE after 6-hr culture (n = 4).
Data represent mean ± SEM. See also Figure S5.

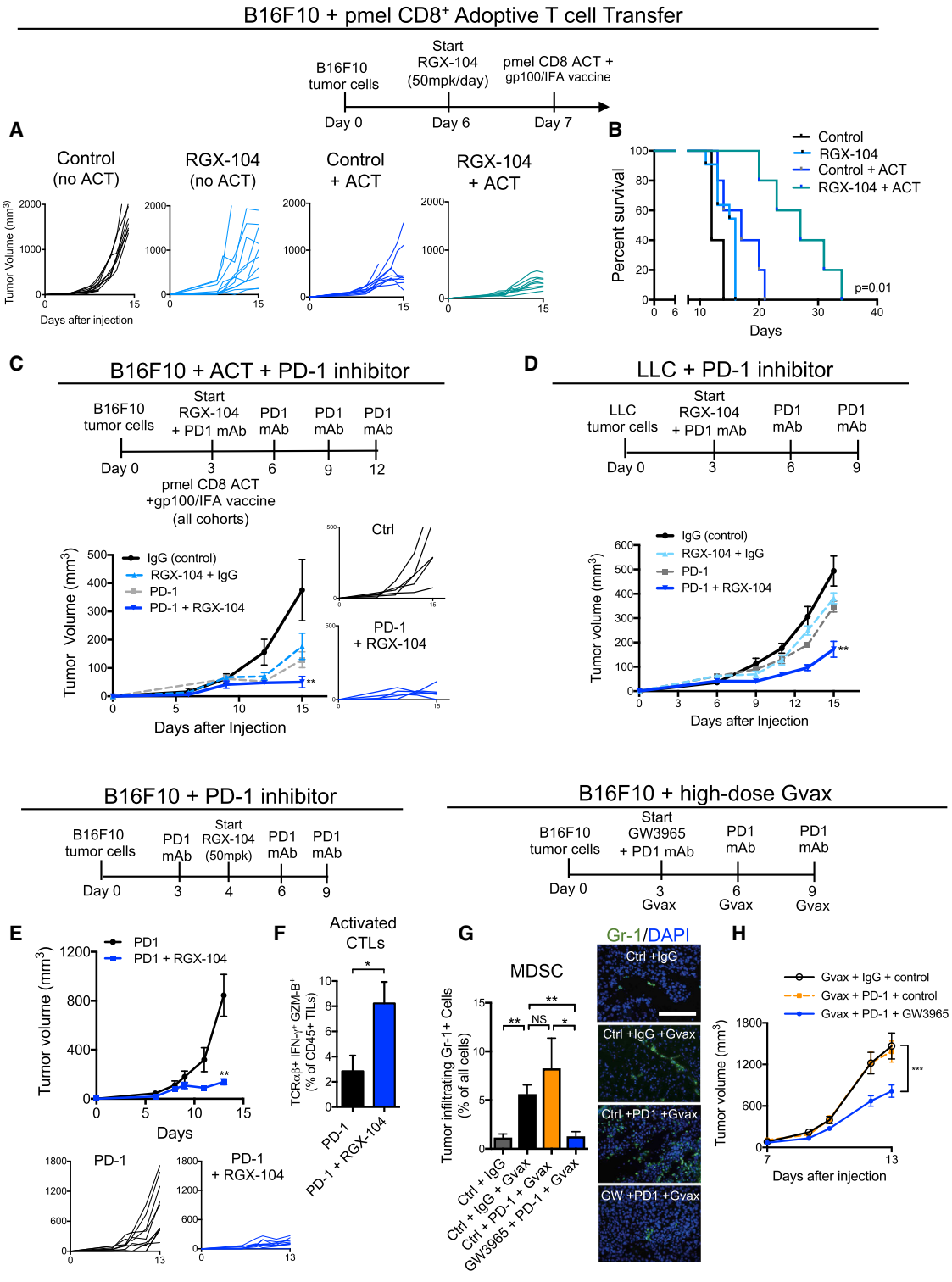

Figure 6. LXR Agonism Provides Additive Anti-tumor Efficacy When Combined with Immunotherapy

(A) Therapy regimen schematic (top) and individual tumor volumes of subcutaneous B16F10 tumors. Treatment cohorts include control without adoptive T cell transfer (ACT), RGX-104 (50 mg/kg) without ACT, control with ACT and gp100 vaccination, and RGX-104 (50 mg/kg) with ACT and gp100 vaccination. 2×10^6 $CD8^+$ T cells from Pmel mice were transferred per recipient ($n \geq 5$).

(B) Survival data at 34 days of B16F10 tumor-bearing mice treated with ACT and gp100 vaccination, RGX-104 (50 mg/kg), or ACT and gp100 vaccination in combination with RGX-104 (50 mg/kg) compared with the control ($n \geq 5$).

(legend continued on next page)

also significantly elevated (Figures 6G and 6H). Importantly, addition of the LXR agonist to anti-PD-1, even in the context of Gvax, significantly reduced tumoral MDSCs to baseline levels and significantly impaired tumor growth in this resistant model (Figures 6G and 6H). These findings demonstrate that combined LXR agonist/anti-PD-1 therapy can augment T cell activation beyond that achieved with single-agent anti-PD-1 therapy in poorly immunogenic resistant models.

LXR Agonist Therapy Depletes MDSCs in Human Cancer Patients and Elicits T Cell Activation

RGX-104 is currently in an ongoing multicenter dose escalation phase 1 trial in patients with metastatic solid cancers or lymphomas that have progressed on standard of care regimens, including immune checkpoint inhibitor therapy (ClinicalTrials.gov, NCT02922764). Peripheral blood samples of patients were obtained prior to initiation of dosing and at weekly intervals when RGX-104 was administered as a single agent on days 1–21 of a 28-day cycle. Blood samples were collected by care providers, and processing and flow cytometric analyses were conducted by an independent contract research laboratory. As expected, the gating strategy used for quantifying human MDSCs ($CD15^+CD33^+CD11b^+CD14^-HLA\text{-}DR^{low}$ cells; Figures S6A and S6B) revealed higher numbers of MDSCs in the peripheral blood of cancer patients enrolled in the phase 1 trial relative to healthy volunteers (Figure 7A). Additionally, pre-treatment circulating MDSC levels positively correlated with the abundance of tumor-infiltrating MDSCs in available paired tumor biopsies obtained from patients (Figure S6D). Remarkably, the abundance of G-MDSCs in the first six evaluable patients enrolled in the trial—harboring melanoma, sarcoma, and renal, uterine, and colorectal cancers—significantly decreased upon oral LXR agonist treatment (Figures 7B–7D). Peak G-MDSC depletion (median 86% decrease, mean 85%) was observed 2–3 weeks after initiation of therapy. In some patients, G-MDSC levels rebounded modestly during the off-treatment week, with a subsequent reduction during the next cycle of treatment (Figure 7B). M-MDSCs ($CD14^+Lin^{neg}HLA\text{-}DR^{low}$) also exhibited reduced abundance 2–3 weeks after RGX-104 treatment initiation relative to pre-dose levels in 5 of 6 patients (median 33% decrease, mean 42%; Figure 7E); however, G-MDSC depletion was more pronounced (Figure 7D). Both G-MDSCs and M-MDSCs expressed high levels of PD-L1, further confirming that these cells are *bona fide* MDSCs (Figure S6E). Interestingly, G-MDSCs had more substantial expression of PD-L1 on average (Figure S6E), suggesting that they might be more potent mediators of resistance to checkpoint blockade in these patients' tumor types. Importantly, the observed significant declines in MDSC levels in these patients were not associated with significant changes in other key hematologic cell populations. Specifically, the mean peak change in total white blood cell, absolute neutrophil, absolute lymphocyte, and absolute monocyte counts in these patients were −16%, −17%, +6%, and +7%, respectively, within the first 2 weeks of RGX-104 treatment and normalized during the 4-week cycle. Of note, RGX-104 was well tolerated in these six patients, with no dose-limiting toxicities. These findings reveal that LXR activation significantly depleted MDSCs in cancer patients harboring a variety of metastatic cancers.

Consistent with our observations in mice, treatment of patients with RGX-104 was associated with a significant increase in CTL activation, as revealed by substantial increases in the fraction of $CD8^+$ T cells expressing glucocorticoid-induced TNFR-related (GITR)—a marker of T cell activation observed to be expressed by tumor-antigen specific T cells (Durham et al., 2017)—in the circulation of 5 of 6 patients (median 224% increase, mean 213%; Figures 7F and S6F). T cell activation occurred predominantly in the $PD\text{-}1^+$ $CD8^+$ population after therapy with RGX-104 (median 322% increase, mean 352%; Figures 7G and 7H), consistent with this population of cells possessing the "exhausted" phenotype that has been associated with tumor-targeting cytotoxic T cells—the main target cell population activated with checkpoint blockade (Huang et al., 2017; Kamphorst et al., 2017; Wei et al., 2017).

DISCUSSION

During cancer progression, malignant cells exploit multiple mechanisms to evade immune-mediated detection and elimination (Plitas and Rudensky, 2016). A large body of literature has associated MDSCs with immune suppression, cancer progression, and adverse outcomes. Some cytotoxic chemotherapies have been observed to reduce circulating MDSC levels

(C) Therapy regimen schematic (top), mean tumor volume (left), and individual tumor growth curves (right) of subcutaneous B16F10 tumors. Treatment cohorts include RGX-104 (100 mg/kg) with control antibody isotype-matched to anti-PD-1, anti-PD-1, and anti-PD-1 with RGX-104 (100 mg/kg) compared with control (control antibody isotype-matched to anti-PD-1). All cohorts received ACT of 2×10^6 $CD8^+$ T cells from Pmel mice per recipient as well as gp100 vaccination 3 days after tumor injections (n = 7).

(D) Therapy regimen (top) and mean tumor volume of subcutaneous Lewis lung carcinoma (LLC) tumors. Treatment cohorts included RGX-104 (100 mg/kg) with control antibody isotype-matched to anti-PD-1, anti-PD-1, and anti-PD-1 with RGX-104 (100 mg/kg) compared with control (control antibody isotype-matched to anti-PD-1) (n = 7).

(E) Therapy regimen schematic (top), mean tumor volume (left), and individual tumor growth curves (below) of subcutaneous B16F10 tumors treated with anti-PD-1 monoclonal antibody or anti-PD-1 with RGX-104 (50 mg/kg) (n = 5).

(F) Percentage of $TCR\alpha\beta^+IFN\text{-}\gamma^+GZM\text{-}B^+$-expressing cytotoxic T cells of total $CD45^+$ TILs from B16F10 tumors treated with anti-PD-1 or anti-PD-1 in combination with RGX-104 (50 mg/kg) as described in (E) (n = 5).

(G) Therapy regimen (top) and quantification (left) and representative immunofluorescence images of tumor-infiltrating $Gr\text{-}1^+$ cells within subcutaneous B16F10 tumors. Treatment cohorts included Gvax with control antibody isotype-matched to anti-PD-1, Gvax with anti-PD-1, and Gvax with anti-PD-1 and GW3965 (100 mg/kg) compared with control (control antibody isotype-matched to anti-PD-1) (n = 6). Scale bar, 143 μm.

(H) Mean tumor volumes of B16F10 subcutaneous tumors from the cohorts described in (G). Cohorts included Gvax with control antibody isotype-matched to anti-PD-1, Gvax with anti-PD-1, and Gvax with anti-PD-1 and GW3965 (100 mg/kg) (n = 6).

Data represent mean ± SEM.

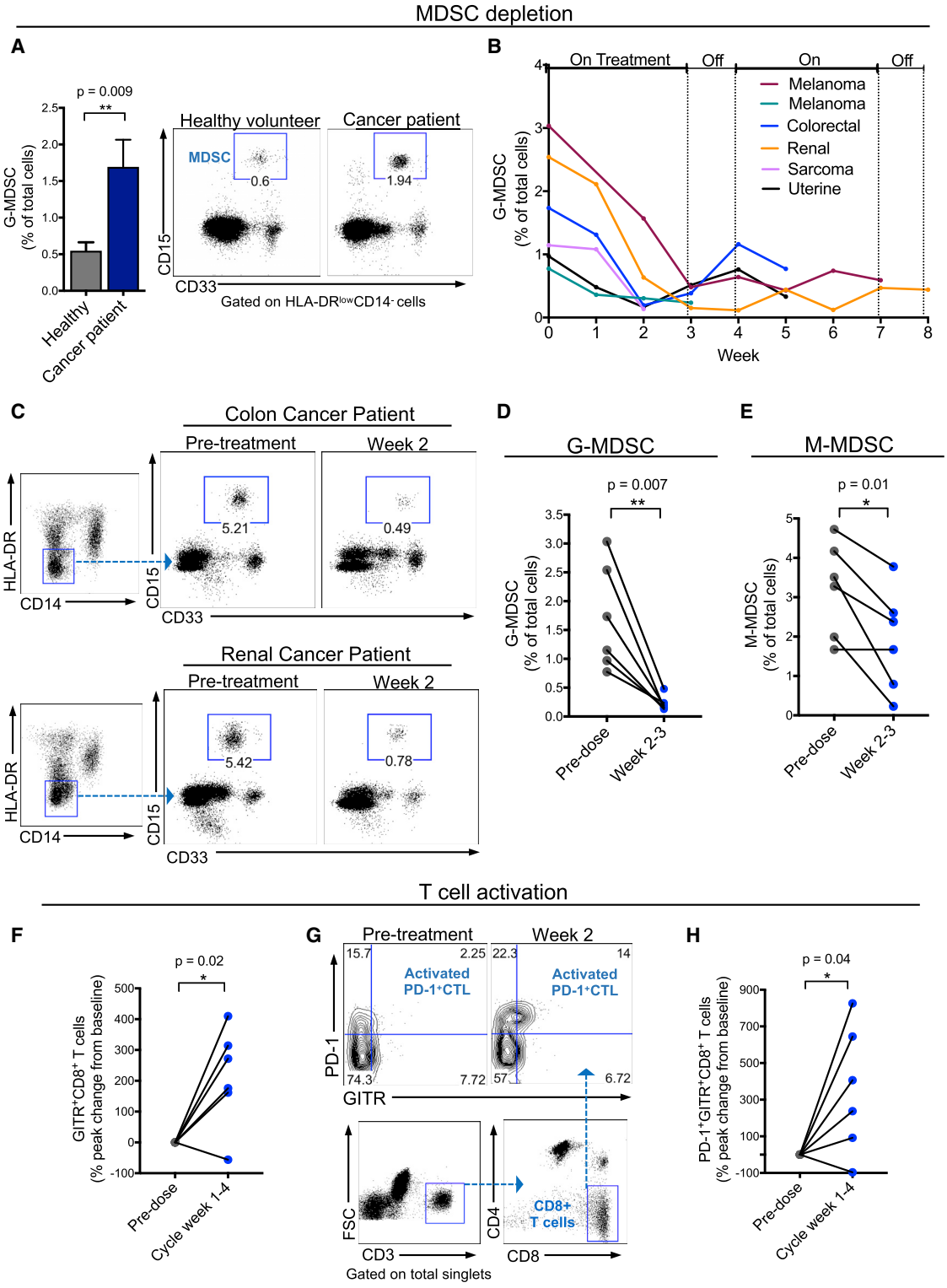

Figure 7. RGX-104 Depletes MDSCs and Activates CD8+ T Cells in Human Cancer Patients

(A) Percentage of G-MDSCs of total circulating cells in the peripheral blood of cancer patients relative to healthy volunteers (n ≥ 6). Shown are representative plots demonstrating the G-MDSC population in healthy volunteers compared with cancer patients.

(B) Percent of G-MDSCs of total circulating cells measured weekly from six patients treated with two 28-day cycles of RGX-104 (administered once daily for 3 weeks and then off for one week); week 0 corresponds to immediately prior to treatment initiation. For some patients, data are not available for the entire two cycles because of lack of blood samples or treatment termination (n = 6).

(legend continued on next page)

(Welters et al., 2016) and are now believed to contribute in part to anti-tumor effects of certain regimens. Such observations have heightened interest in selective and potent targeting of these immune suppressive cells. Our data describing that LXR/ApoE signaling reduces the survival and abundance of MDSCs *in vitro* and *in vivo*, thereby driving T cell responses, constitutes a basis for testing this approach as a means of augmenting anti-tumor immunity. Given that LXR-mediated *Apoe* induction promotes anti-tumor immunity, one would expect selection against ApoE protein expression in the tumor microenvironment. Indeed, our previous work revealed that metastatic melanoma cells silence *Apoe* expression via overexpression of multiple microRNAs, leading to reduced ApoE protein abundance in the tumor microenvironment (Pencheva et al., 2012). Although our results demonstrate that ApoE can directly repress MDSC survival via the LRP8 receptor, we cannot rule out additional direct or indirect effects of LXR/ApoE signaling on MDSCs that may affect the abundance of this population.

LXRs are activated by oxysterols and regulate cholesterol and lipid metabolism. Consistent with our findings of a role for LXR signaling in tumor immunology, *LXR* gene variants have been associated with human immunologic disorders, including inflammatory bowel disease (Andersen et al., 2011), systemic lupus erythematosus (Jeon et al., 2014), and altered susceptibility to tuberculosis (Han et al., 2014). Nevertheless, the exact role of LXR signaling in these processes remains unclear. Past studies have implicated LXRs in both suppressing (Bensinger et al., 2008; Zelcer et al., 2007) and promoting (Fontaine et al., 2007; Landis et al., 2002) inflammatory responses. These differences have been attributed to the context within which LXR agonism was studied, the cell types affected (Waddington et al., 2015), as well as the duration of LXR activation (Fontaine et al., 2007). Interestingly, LXR agonism has been reported previously to increase macrophage-mediated phagocytosis of mature neutrophils, providing another path by which LXRs could affect a myeloid cell type (Hong et al., 2012).

The strong anti-tumor responses observed in immunocompetent mice and in mice solely possessing innate immunity are consistent with the suppressive effects of MDSCs on adaptive (T cell) and innate (natural killer [NK] cell) responses as well as known direct tumor-promoting effects of MDSCs via secretion of pro-tumorigenic molecules. We observed that LXR activation induced $CD8^+$ T cell responses in human cancer patients harboring diverse tumor types, including generally described ''immune-cold'' malignancies such as microsatellite stable colon cancer. Additionally, T cell activation was observed in patients harboring classically defined immunologically sensitive tumor types, such as renal cancer and melanoma, even in the setting of prior resistance to checkpoint inhibitor therapy. Moreover, combined LXR activation and PD-1 inhibition elicited additive or synergistic anti-tumor responses in mouse models, consistent with augmented T cell responses being elicited upon restrained myeloid immune suppression (Jeon et al., 2014). Our observations reveal that LXR targeting represents a new strategy for repressing innate immune suppression and augmenting anti-tumor immunity. To the best of our knowledge, RGX-104 represents the first MDSC-targeting therapeutic agent that sufficiently curbs immune suppression as a single agent to elicit CTL activation in humans. These findings suggest that LXR activation may be effective at preventing metastasis formation and inhibiting progression of metastatic disease, given its multi-mechanistic effects on curbing immune suppression, angiogenesis, and tumor invasion. Additionally, LXR therapy may augment anti-tumor responses when given in combination with checkpoint inhibitors or adoptive T cell therapies or may render patients who are refractory to these immunotherapies responsive.

ApoE has been previously associated with both pro-inflammatory and anti-inflammatory responses in various pathological contexts. In atherosclerosis, ApoE loss was found to enhance the expression of inflammatory markers on macrophages or foam cells and contribute to atherosclerosis progression (Hansson, 2001; White et al., 2014). In contrast, ApoE loss has also been shown to impair inflammatory responses to pathogenic infections, including *L. monocytogenes*, *K. pneumonia*, and *M. tuberculosis* (Zhang et al., 2011). Similar to these latter observations in microbial pathogenesis, our findings in cancer revealed that ApoE genetic inactivation impairs immunity via MDSC accumulation. The complex nature of various disease-associated inflammatory responses as well as the heterogeneity of inflammatory pathology, especially among distinct cancer types, highlight the need for an enhanced understanding of the effect of ApoE signaling on specific immune cell populations in the contexts of various pathologic processes.

Our observations regarding the role ApoE plays in regulating MDSCs in cancer as well as ApoE-dependent regulation of myeloid cells in non-tumor-bearing mice suggest the possibility that ApoE signaling and ApoE variants may affect pathogenic immature myeloid populations in other ApoE-dependent pathologic processes. Future studies are warranted to study the potential roles of these innate myeloid cells in the etiology of other such disorders. In summary, our findings uncover a critical

(C) Representative plots demonstrating the G-MDSC population in a colorectal cancer patient (top) and a renal cancer patient (bottom) treated with RGX-104 at week 0 (pre-treatment) compared with 2 weeks after therapy initiation.
(D and E) Percentage of G-MDSCs (D) and M-MDSCs (E) of total circulating cells in 6 patients treated with RGX-104 at week 0 compared with weeks 2–3 on therapy (n = 6).
(F) Percentage of peak change in $CD8^+$ T cells that express GITR of total $CD8^+$ T cells in the circulation of patients treated with RGX-104 at week 0 compared with weeks 1–4 of the therapy cycle (n = 6).
(G) Representative plot showing the population of PD-1^+GITR$^+$ double-positive $CD8^+$ T cells (activated PD-1^+ CTLs) in the circulation of a patient treated with RGX-104 at week 0 (pre-treatment) and at week 2 of therapy.
(H) Percentage of peak change in $CD8^+$ T cells that are double-positive for PD-1^+GITR$^+$ in the circulation of patients treated with RGX-104 at week 0 compared with weeks 1–4 of the therapy cycle (n = 6).
Data represent mean ± SEM. See also Figure S6.

role for LXR/ApoE/LRP8 signaling in the regulation of anti-tumor immunity.

STAR★METHODS

Detailed methods are provided in the online version of this paper and include the following:

- KEY RESOURCES TABLE
- CONTACT FOR REAGENT AND RESOURCE SHARING
- EXPERIMENTAL MODEL AND SUBJECT DETAILS
  - Cell culture
  - Animal Models
  - Patient Details
- METHOD DETAILS
  - Isolation of tumor-infiltrating immune cells
  - Tumor Flow Cytometry
  - Isolation of MDSCs
  - MDSC *in vitro* Proliferation Assay
  - MDSC Adhesion Assay
  - *In Vitro* MDSC Apoptosis Assay
  - MDSC mRNA sequencing library preparation
  - T Cell *Ex vivo* Suppression Assay
  - Isolation of Pmel $CD8^+$ T cells and Adoptive Transfer
  - Immunohistochemistry
  - *In vitro* MDSC differentiation assay
  - MDSC adoptive transfer
  - ApoE Protein Production
  - Mouse Genotyping
  - Lentiviral shRNA-Based Apoe Gene Knockdown
  - Human MDSC and T cell Flow Cytometry Analysis
  - Clinical Study Design
  - Clinical Assessments
- QUANTIFICATION AND STATISTICAL ANALYSIS
  - Data Analysis

SUPPLEMENTAL INFORMATION

Supplemental Information includes six figures and can be found with this article online at https://doi.org/10.1016/j.cell.2017.12.026.

ACKNOWLEDGMENTS

We are grateful to members of our laboratory for providing insightful comments on past versions of this manuscript. *Apoe* null mice were generously provided by Jan Breslow. LXR mutant mice were generously provided by David Mangelsdorf, who also provided insights into LXR biology. The GL261 glioblastoma cell line was kindly provided by Paul Davis. We thank Saeed Tavazoie and David Darst for intellectual and operational guidance in RGX-104 development. We thank Scott Spector for logistical oversight of RGX-104 clinical operations. We thank Lisa Noble, Helen Tian, and Katya Leites for assistance with experiments. We thank Alexander Lesokhin for advice regarding human sample flow cytometry analyses. We thank the Serametrix Corporation for performing timely flow cytometry analysis of patient blood samples. The research of S.F.T. was supported in part by a Faculty Scholar grant from the Howard Hughes Medical Institute and by the DOD Collaborative Scholars and Innovators Award (grant W81XWH-12-1-0301), a Pershing Square Sohn award, a Breast Cancer Research Foundation grant, and NIH grant R01CA184804-01A2. The research reported in this publication was supported by the NCI of the NIH under award 1R44CA206677-01A1. B.N.O. was supported by a Deutsche Forschungsgemeinschaft postdoctoral fellowship (grant OS 498/1-1).

AUTHOR CONTRIBUTIONS

M.F.T. and S.F.T. conceived the project and supervised all research. M.F.T. and D.M. designed and oversaw the immune profiling and flow cytometry experiments. M.F.T., B.S.R., and D.M. designed the flow cytometry panels and parameters. M.F.T. and S.F.T. wrote the manuscript, and D.M. provided insightful edits. M.F.T., I.P., R.T., B.N.O., J.P., F.C.G., I.K., C.A.-A., M.L.D., C.Z., S.T., and E.A.M. designed, performed, and analyzed the experiments. M.M., A.M., B.C., M.A.P., A.R., E.R., and R.J.W. directed the treatment of cancer patients with RGX-104. M.M., A.M., B.C., and M.A.P. served as clinical investigators of the phase 1 trial of RGX-104. E.R., M.S., and S.F.T. contributed to the design of the RGX-104 phase 1 clinical trial.

DECLARATION OF INTERESTS

M.F.T. and S.F.T. are co-founders and shareholders of Rgenix and members of its scientific advisory board, and M.F.T., I.K., F.C.G., C.A.-A., M.S., R.W., S.T., and E.R. are shareholders and current employees of Rgenix. A.R. and D.M. are advisors and shareholders of Rgenix. S.F.T. holds patent 9,526,710 related to this work.

Received: August 25, 2017
Revised: November 14, 2017
Accepted: December 19, 2017
Published: January 18, 2018

REFERENCES

Almand, B., Clark, J.I., Nikitina, E., van Beynen, J., English, N.R., Knight, S.C., Carbone, D.P., and Gabrilovich, D.I. (2001). Increased production of immature myeloid cells in cancer patients: a mechanism of immunosuppression in cancer. J. Immunol. *166*, 678–689.

Andersen, V., Christensen, J., Ernst, A., Jacobsen, B.A., Tjønneland, A., Krarup, H.B., and Vogel, U. (2011). Polymorphisms in NF-κB, PXR, LXR, PPARγ and risk of inflammatory bowel disease. World J. Gastroenterol. *17*, 197–206.

Apfel, R., Benbrook, D., Lernhardt, E., Ortiz, M.A., Salbert, G., and Pfahl, M. (1994). A novel orphan receptor specific for a subset of thyroid hormone-responsive elements and its interaction with the retinoid/thyroid hormone receptor subfamily. Mol. Cell. Biol. *14*, 7025–7035.

Bensinger, S.J., Bradley, M.N., Joseph, S.B., Zelcer, N., Janssen, E.M., Hausner, M.A., Shih, R., Parks, J.S., Edwards, P.A., Jamieson, B.D., and Tontonoz, P. (2008). LXR signaling couples sterol metabolism to proliferation in the acquired immune response. Cell *134*, 97–111.

Curran, M.A., and Allison, J.P. (2009). Tumor vaccines expressing flt3 ligand synergize with ctla-4 blockade to reject preimplanted tumors. Cancer Res. *69*, 7747–7755.

Curran, M.A., Montalvo, W., Yagita, H., and Allison, J.P. (2010). PD-1 and CTLA-4 combination blockade expands infiltrating T cells and reduces regulatory T and myeloid cells within B16 melanoma tumors. Proc. Natl. Acad. Sci. USA *107*, 4275–4280.

Davila, M.L., and Brentjens, R.J. (2016). CD19-Targeted CAR T cells as novel cancer immunotherapy for relapsed or refractory B-cell acute lymphoblastic leukemia. Clin. Adv. Hematol. Oncol. *14*, 802–808.

Dieckmann, M., Dietrich, M.F., and Herz, J. (2010). Lipoprotein receptors–an evolutionarily ancient multifunctional receptor family. Biol. Chem. *391*, 1341–1363.

Durham, N.M., Holoweckyj, N., MacGill, R.S., McGlinchey, K., Leow, C.C., and Robbins, S.H. (2017). GITR ligand fusion protein agonist enhances the tumor antigen-specific CD8 T-cell response and leads to long-lasting memory. J. Immunother. Cancer *5*, 47.

Evans, R.M., and Mangelsdorf, D.J. (2014). Nuclear Receptors, RXR, and the Big Bang. Cell *157*, 255–266.

Fontaine, C., Rigamonti, E., Nohara, A., Gervois, P., Teissier, E., Fruchart, J.C., Staels, B., and Chinetti-Gbaguidi, G. (2007). Liver X receptor activation potentiates the lipopolysaccharide response in human macrophages. Circ. Res. *101*, 40–49.

Gabrilovich, D.I., Ostrand-Rosenberg, S., and Bronte, V. (2012). Coordinated regulation of myeloid cells by tumours. Nat. Rev. Immunol. *12*, 253–268.

Gros, A., Robbins, P.F., Yao, X., Li, Y.F., Turcotte, S., Tran, E., Wunderlich, J.R., Mixon, A., Farid, S., Dudley, M.E., et al. (2014). PD-1 identifies the patient-specific $CD8^+$ tumor-reactive repertoire infiltrating human tumors. J. Clin. Invest. *124*, 2246–2259.

Grzes, K.M., Field, C.S., and Pearce, E.J. (2017). Treg Cells Survive and Thrive in Inhospitable Environments. Cell Metab. *25*, 1213–1215.

Han, M., Liang, L., Liu, L.R., Yue, J., Zhao, Y.L., and Xiao, H.P. (2014). Liver X receptor gene polymorphisms in tuberculosis: effect on susceptibility. PLoS ONE *9*, e95954.

Hansson, G.K. (2001). Regulation of immune mechanisms in atherosclerosis. Ann. NY Acad. Sci. *947*, 157–165, discussion 165–166.

Hong, C., and Tontonoz, P. (2014). Liver X receptors in lipid metabolism: opportunities for drug discovery. Nat. Rev. Drug Discov. *13*, 433–444.

Hong, C., Kidani, Y., A-Gonzalez, N., Phung, T., Ito, A., Rong, X., Ericson, K., Mikkola, H., Beaven, S.W., Miller, L.S., et al. (2012). Coordinate regulation of neutrophil homeostasis by liver X receptors in mice. J. Clin. Invest. *122*, 337–347.

Huang, A.C., Postow, M.A., Orlowski, R.J., Mick, R., Bengsch, B., Manne, S., Xu, W., Harmon, S., Giles, J.R., Wenz, B., et al. (2017). T-cell invigoration to tumour burden ratio associated with anti-PD-1 response. Nature *545*, 60–65.

Hui, E., Cheung, J., Zhu, J., Su, X., Taylor, M.J., Wallweber, H.A., Sasmal, D.K., Huang, J., Kim, J.M., Mellman, I., and Vale, R.D. (2017). T cell costimulatory receptor CD28 is a primary target for PD-1-mediated inhibition. Science *355*, 1428–1433.

Iwai, Y., Terawaki, S., and Honjo, T. (2005). PD-1 blockade inhibits hematogenous spread of poorly immunogenic tumor cells by enhanced recruitment of effector T cells. Int. Immunol. *17*, 133–144.

Jeon, J.Y., Nam, J.Y., Kim, H.A., Park, Y.B., Bae, S.C., and Suh, C.H. (2014). Liver X receptors alpha gene (NR1H3) promoter polymorphisms are associated with systemic lupus erythematosus in Koreans. Arthritis Res. Ther. *16*, R112.

Kamphorst, A.O., Pillai, R.N., Yang, S., Nasti, T.H., Akondy, R.S., Wieland, A., Sica, G.L., Yu, K., Koenig, L., Patel, N.T., et al. (2017). Proliferation of PD-1+ CD8 T cells in peripheral blood after PD-1-targeted therapy in lung cancer patients. Proc. Natl. Acad. Sci. USA *114*, 4993–4998.

Krummel, M.F., and Allison, J.P. (1995). CD28 and CTLA-4 have opposing effects on the response of T cells to stimulation. J. Exp. Med. *182*, 459–465.

Landis, M.S., Patel, H.V., and Capone, J.P. (2002). Oxysterol activators of liver X receptor and 9-cis-retinoic acid promote sequential steps in the synthesis and secretion of tumor necrosis factor-alpha from human monocytes. J. Biol. Chem. *277*, 4713–4721.

Leach, D.R., Krummel, M.F., and Allison, J.P. (1996). Enhancement of antitumor immunity by CTLA-4 blockade. Science *271*, 1734–1736.

Lim, W.A., and June, C.H. (2017). The Principles of Engineering Immune Cells to Treat Cancer. Cell *168*, 724–740.

Lin, C.Y., and Gustafsson, J.A. (2015). Targeting liver X receptors in cancer therapeutics. Nat. Rev. Cancer *15*, 216–224.

Meyer, C., Cagnon, L., Costa-Nunes, C.M., Baumgaertner, P., Montandon, N., Leyvraz, L., Michielin, O., Romano, E., and Speiser, D.E. (2014). Frequencies of circulating MDSC correlate with clinical outcome of melanoma patients treated with ipilimumab. Cancer Immunol. Immunother. *63*, 247–257.

Nelson, E.R., Wardell, S.E., Jasper, J.S., Park, S., Suchindran, S., Howe, M.K., Carver, N.J., Pillai, R.V., Sullivan, P.M., Sondhi, V., et al. (2013). 27-Hydroxycholesterol links hypercholesterolemia and breast cancer pathophysiology. Science *342*, 1094–1098.

Okazaki, T., and Honjo, T. (2007). PD-1 and PD-1 ligands: from discovery to clinical application. Int. Immunol. *19*, 813–824.

Overwijk, W.W., Tsung, A., Irvine, K.R., Parkhurst, M.R., Goletz, T.J., Tsung, K., Carroll, M.W., Liu, C., Moss, B., Rosenberg, S.A., and Restifo, N.P. (1998). gp100/pmel 17 is a murine tumor rejection antigen: induction of "self"-reactive, tumoricidal T cells using high-affinity, altered peptide ligand. J. Exp. Med. *188*, 277–286.

Peggs, K.S., Quezada, S.A., and Allison, J.P. (2008). Cell intrinsic mechanisms of T-cell inhibition and application to cancer therapy. Immunol. Rev. *224*, 141–165.

Pencheva, N., Tran, H., Buss, C., Huh, D., Drobnjak, M., Busam, K., and Tavazoie, S.F. (2012). Convergent multi-miRNA targeting of ApoE drives LRP1/LRP8-dependent melanoma metastasis and angiogenesis. Cell *151*, 1068–1082.

Pencheva, N., Buss, C.G., Posada, J., Merghoub, T., and Tavazoie, S.F. (2014). Broad-spectrum therapeutic suppression of metastatic melanoma through nuclear hormone receptor activation. Cell *156*, 986–1001.

Plitas, G., and Rudensky, A.Y. (2016). Regulatory T Cells: Differentiation and Function. Cancer Immunol. Res. *4*, 721–725.

Sharma, P., Hu-Lieskovan, S., Wargo, J.A., and Ribas, A. (2017). Primary, Adaptive, and Acquired Resistance to Cancer Immunotherapy. Cell *168*, 707–723.

Shipp, C., Speigl, L., Janssen, N., Martens, A., and Pawelec, G. (2016). A clinical and biological perspective of human myeloid-derived suppressor cells in cancer. Cell. Mol. Life Sci. *73*, 4043–4061.

Sinha, P., Clements, V.K., Bunt, S.K., Albelda, S.M., and Ostrand-Rosenberg, S. (2007). Cross-talk between myeloid-derived suppressor cells and macrophages subverts tumor immunity toward a type 2 response. J. Immunol. *179*, 977–983.

Tall, A.R., and Yvan-Charvet, L. (2015). Cholesterol, inflammation and innate immunity. Nat. Rev. Immunol. *15*, 104–116.

Tumeh, P.C., Harview, C.L., Yearley, J.H., Shintaku, I.P., Taylor, E.J., Robert, L., Chmielowski, B., Spasic, M., Henry, G., Ciobanu, V., et al. (2014). PD-1 blockade induces responses by inhibiting adaptive immune resistance. Nature *515*, 568–571.

Villa, G.R., Hulce, J.J., Zanca, C., Bi, J., Ikegami, S., Cahill, G.L., Gu, Y., Lum, K.M., Masui, K., Yang, H., et al. (2016). An LXR-Cholesterol Axis Creates a Metabolic Co-Dependency for Brain Cancers. Cancer Cell *30*, 683–693.

Waddington, K.E., Jury, E.C., and Pineda-Torra, I. (2015). Liver X receptors in immune cell function in humans. Biochem. Soc. Trans. *43*, 752–757.

Weber, J., Gibney, G., Kudchadkar, R., Yu, B., Cheng, P., Martinez, A.J., Kroeger, J., Richards, A., McCormick, L., Moberg, V., et al. (2016). Phase I/II Study of Metastatic Melanoma Patients Treated with Nivolumab Who Had Progressed after Ipilimumab. Cancer Immunol. Res. *4*, 345–353.

Wei, S.C., Levine, J.H., Cogdill, A.P., Zhao, Y., Anang, N.A.S., Andrews, M.C., Sharma, P., Wang, J., Wargo, J.A., Pe'er, D., et al. (2017). Distinct Cellular Mechanisms Underlie Anti-CTLA-4 and Anti-PD-1 Checkpoint Blockade. Cell *170*, 1120–1133.e17.

Welters, M.J., van der Sluis, T.C., van Meir, H., Loof, N.M., van Ham, V.J., van Duikeren, S., Santegoets, S.J., Arens, R., de Kam, M.L., Cohen, A.F., et al. (2016). Vaccination during myeloid cell depletion by cancer chemotherapy fosters robust T cell responses. Sci. Transl. Med. *8*, 334ra52.

White, C.R., Garber, D.W., and Anantharamaiah, G.M. (2014). Anti-inflammatory and cholesterol-reducing properties of apolipoprotein mimetics: a review. J. Lipid Res. *55*, 2007–2021.

Willy, P.J., Umesono, K., Ong, E.S., Evans, R.M., Heyman, R.A., and Mangelsdorf, D.J. (1995). LXR, a nuclear receptor that defines a distinct retinoid response pathway. Genes Dev. *9*, 1033–1045.

Wrzesinski, C., Paulos, C.M., Kaiser, A., Muranski, P., Palmer, D.C., Gattinoni, L., Yu, Z., Rosenberg, S.A., and Restifo, N.P. (2010). Increased intensity lymphodepletion enhances tumor treatment efficacy of adoptively transferred tumor-specific T cells. J. Immunother. *33*, 1–7.

Youn, J.I., Nagaraj, S., Collazo, M., and Gabrilovich, D.I. (2008). Subsets of myeloid-derived suppressor cells in tumor-bearing mice. J. Immunol. *181*, 5791–5802.

Zelcer, N., Khanlou, N., Clare, R., Jiang, Q., Reed-Geaghan, E.G., Landreth, G.E., Vinters, H.V., and Tontonoz, P. (2007). Attenuation of neuroinflammation and Alzheimer's disease pathology by liver x receptors. Proc. Natl. Acad. Sci. USA *104*, 10601–10606.

Zhang, H., Wu, L.M., and Wu, J. (2011). Cross-talk between apolipoprotein E and cytokines. Mediators Inflamm. *2011*, 949072.

Please cite this article in press as: Tavazoie et al., LXR/ApoE Activation Restricts Innate Immune Suppression in Cancer, Cell (2018), https://doi.org/10.1016/j.cell.2017.12.026

STAR★METHODS

KEY RESOURCES TABLE

REAGENT or RESOURCE	SOURCE	IDENTIFIER
Antibodies		
Brilliant Violet 785 CD45 (30-F11)	Biolegend	Cat# 103149
Brilliant Violet 605 CD11b (M1/70)	Biolegend	Cat# 101257
Brilliant Violet 711 Ly-6C (HK1.4)	Biolegend	Cat# 128037
PerCP-Cy5.5 Ly-6G (1A8)	BD PharMingen	Cat# 560602
Brilliant Violet 421 MHCII (M5/114.15.2)	Biolegend	Cat# 107631
PE CD24 (M1/69)	Biolegend	Cat# 101807
FITC F4/80 (BM8)	Biolegend	Cat# 123107
PE/Cy7 CD86 (GL-1)	Biolegend	Cat# 105013
APC CD103 (2E7)	Biolegend	Cat# 121413
Zombie NIR	Biolegend	Cat# 423105
Cleaved Caspase-3 (Asp175)	Cell Signaling	Cat# 9661
*In Vivo*Mab anti mouse PD-1 (RMP1-14)	BioXCell	Cat# BE0146
Alexa Fluor 700 CD8a (53-6.7)	eBioscience	Cat# 56-0081-82
PE/Cy7 IFNg (XMG1.2)	eBioscience	Cat# 25-7311-41
FITC Granzyme B (NGZB)	eBioscience	Cat# 11-8898-82
FITC CD11b (M1/70)	Biolegend	Cat# 101205
FITC CD19 (1D3/CD19)	Biolegend	Cat# 152404
Brilliant Violet 605 CD4 (GK1.5)	Biolegend	Cat# 100451
Brilliant Violet 421 CD279 (PD-1) (29F.1A12)	Biolegend	Cat# 135221
PerCP-Cy5.5 TCRbeta	Biolegend	Cat# 109228
PE Granzyme B	eBioscience	Cat# 12-8899-41
PE CD69	Biolegend	Cat# 10450
PE/Cy7 CD45	eBioscience	Cat# 25-0451-82
PB IFNg	eBioscience	Cat# 48-7311-82
Aqua	Invitrogen	Cat# L34957
Fc Block	BioLegend	Cat# 101320
CD279 (PD-1) Monoclonal Antibody (MIH4), PE	eBioscience	Cat# 12-9969-42
Purified anti-human CD357 (GITR) Antibody	BioLegend	Cat# 371202
FITC Mouse Anti-Human CD15	BD Biosciences	Cat# 560997
Purified anti-CD33 Antibody	BioLegend	Cat# 825601
BV421 Mouse Anti-Human CD274	BD Biosciences	Cat# 563738
Bacterial Strain		
Rosetta (DE3) Competent Cells	Novagen	Cat# 70954
One Shot TOP10 Chemically Competent E. Coli	Thermo Fisher	Cat# C4040-10
Chemicals, Peptides, and Recombinant Proteins		
gp100 (25-33), human	Eurogentec	Cat# AS-62589
Platinum Taq DNA Polymerase High Fidelity	Life Technologies	Cat# 11304-011
One Shot TOP10 Chemically Competent E. Coli	Thermo Fisher	Cat# C4040-10
Recombinant Mouse Interleukin-2 (IL-2)	Life Technologies	Cat# PMC0021
Collagenase, Type I	Worthington Biochemical Corporation	Cat# LS004196
Collagenase, Type IV	Worthington Biochemical Corporation	Cat# CLS-4

(*Continued on next page*)

Continued

REAGENT or RESOURCE	SOURCE	IDENTIFIER
Dnase I	Roche	Cat# 10104159001
Cell Trace Violet	Thermo Fisher	Cat# C34557
PreScission Protease	GE Healthcare	Cat# 27-0843-01
Percoll PLUS	GE Healthcare	Cat# 17-5445-01
Brefeldin A	Sigma	Cat# B7651
PMA	Sigma	Cat# P8139
Ionomycin	Sigma	Cat# I0634
Poly-L-Lysine	Sigma	Cat# P4707
COG 133	Tocris	Cat # 3405
D-4F peptide (ApoA1 mimetic)	LifeTein	Cat # 287205 (custom synthesis)
gp100 tetramer (APC)	MBL	Cat # TS-M546-2
Freund's Adjuvant (IFA)	Invivogen	Cat# vac-ifa-10
Critical Commercial Assays		
Myeloid-Derived Suppressor Cell Isolation Kit	Miltenyi Biotec	Cat# 130-094-538
CD8a+ T Cell Isolation Kit (mouse)	Miltenyi Biotec	Cat# 130-104-075
LS Columns	Miltenyi Biotec	Cat# 130-042-401
Dynabeads Mouse T-Activator (CD3/CD28)	Life Technologies	Cat# 11456D
Pier High-Capacity Endotoxin Removal Resin	Thermo Fisher	Cat# 88270
GST SpinTrap	GE Life Sciences	Cat# 28-9523-59
Fix/Perm	BD PharMingen	Cat# 554714
Total RNA Purification Kit	Norgen	Cat #17200
Ribo-Zero Gold rRNA Removal Kit	Illumina	Cat # MRZG12324
ScriptSeq v2 RNA-Seq Library Preparation Kit	Epicenter	Cat # SSV21124
ScriptSeq Index PCR Primers	Epicenter	Cat # RSBC10948
RNA Clean & Concentrator −5	Zymo Research	Cat # R1016
Experimental Models: Organisms/Strains		
Mouse: C57BL/6J	The Jackson Laboratory	RRID: IMSR_JAX:000664
Mouse: *Apoe*$^{-/-}$	The Jackson Laboratory	RRID: IMSR_JAX:002052
Mouse: *LRP8*$^{-/-}$	The Jackson Laboratory	RRID: IMSR_JAX:003524
Mouse: *LXR*$\alpha^{-/-}$	The Jackson Laboratory	RRID: IMSR_JAX:013763
Mouse: *LXR*$\beta^{-/-}$	The Jackson Laboratory	RRID: IMSR_JAX:014635
Mouse: Pmel	The Jackson Laboratory	RRID: IMSR_JAX:005023
Mouse: NOD-SCID	The Jackson Laboratory	RRID: IMSR_JAX:001303
Mouse: *Rag*$^{-/-}$	The Jackson Laboratory	RRID: IMSR_JAX:002216
Cell Line: SK-OV-3	ATCC	RRID: CVCL_0532
Cell Line: OVCAR3	ATCC	RRID: CVCL_0465
Cell Line: U118	ATCC	RRID: CVCL_0633
Cell Line: LN229	ATCC	RRID: CVCL_0393
Cell Line: ACHN	ATCC	RRID: CVCL_1067
Cell Line: H460	ATCC	RRID: CVCL_0459
Cell Line: Renca	ATCC	RRID: CVCL_2174
Cell Line: LLC1	ATCC	RRID: CVCL_4358
Cell Line: B16F10	ATCC	RRID: CVCL_0159
Cell Line:MDA-MB-468	ATCC	RRID: CVCL_0419
Cell Line: U251	Sigma Aldrich	RRID:CVCL_0021
Cell Line:GL261	Paul Davis, Albany Medical College	RRID:CVCL_Y003
Cell Line: MC38	Kerafast	CVCL_B288

(*Continued on next page*)

Continued

REAGENT or RESOURCE	SOURCE	IDENTIFIER
Software and Algorithms		
Prism 7	GraphPad	https://www.graphpad.com/scientific-software/prism/
Flow Jo 8.7	FlowJo	https://www.flowjo.com/solutions/flowjo/downloads
CellProfiler-3.0.0	Cell Profiler	http://cellprofiler.org/releases/
Other		
AxioPlan II	Zeiss	N/A
BD LSR II	BD Biosciences	N/A
BD LSRFortessa	BD Biosciences	N/A

CONTACT FOR REAGENT AND RESOURCE SHARING

Further information and requests for reagents and/or data can be directed to the Lead Contact, Sohail F. Tavazoie (stavazoie@mail.rockefeller.edu). Any sharing of materials or data may be subject to material transfer agreements and/or data-sharing agreements per the requirements of the study sponsors.

EXPERIMENTAL MODEL AND SUBJECT DETAILS

Cell culture

SKOV3 (human, female), OVCAR3 (human, female), U118 (human, male), LN229 (human, female), ACHN (human, male), H460 (human, male), Renca (mouse, male), LLC1 (mouse, male), B16F10 (mouse, male), and MDA-MB-468 (human, female) cell lines were obtained from ATCC (Manassas, VA). The U251 cell line (human, male) was obtained from Sigma Aldrich (St. Louis, MO). The GL261 cell line (mouse, male) was provided by Paul Davis (Albany Medical College, NY). The MC38 (mouse, female) cell line was obtained from Kerafast (Boston, MA).

SK-OV-3 cells were maintained in McCoy's 5a Medium Modified from ATCC supplemented with 10% FBS. OVCAR3 cells were maintained in RPMI-1640 Medium from ATCC supplemented with 0.01mg/mL bovine insulin and 20% FBS. U118 cells were maintained in DMEM from ATCC supplemented with 10% FBS. LN229 cells were maintained in DMEM from ATCC supplemented with 5% FBS. ACHN cells were maintained in DMEM from ATCC supplemented with 10% FBS. H460 cells were maintained in RPMI-1640 from ATCC and supplemented with 10% FBS. Renca cells were maintained in ATCC-formulated RPMI-1640 supplemented with 10% FBS, 0.1mM non-essential amino acids (NEAA), 1mM sodium pyruvate, and 2mM L-glutamine. LLC1 cells were maintained in DMEM from ATCC supplemented with 10% FBS. B16F10 cells were maintained in DMEM from ATCC supplemented with 10% FBS. MDA-MB-468 cells were maintained in ATCC-formulated Leibovitz's L-15 Medium supplemented with 10% FBS. U251 cells were maintained in EMEM supplemented with 2uM Glutamine, 1% NEAA, 1mM sodium pyruvate, and 10% FBS. GL261 cells were maintained in DMEM supplemented with 10% FBS. MC38 cells were maintained in DMEM supplemented with 10% FBS, 2mM glutamine, 0.1mM NEAA, 1mM sodium pyruvate, 10mM HEPES, and 50ug/mL gentamycin sulfate. All cell lines were maintained at 37°C and 5% CO_2.

Animal Models

All mouse experiments and procedures were approved by the Institutional Animal Care and Use Committee (IACUC) at The Rockefeller University. C57BL/6 (JAX stock #000664, RRID: IMSR_JAX:000664), NOD-SCID (JAX stock #001303, RRID: IMSR_JAX:001303), $Rag^{-/-}$ (JAX stock #002216, RRID: IMSR_JAX:002216), and Pmel (B6.Cg-*Thy1*^{a}/Cy Tg(TcraTcrb)8Rest/J) (JAX stock #005023, RRID: IMSR_JAX:005023) mice were purchased from the Jackson Laboratory. *Apoe*$^{-/-}$ (JAX stock #002052, RRID: IMSR_JAX:002052) and *LRP8*$^{-/-}$ (JAX stock #003524, RRID: IMSR_JAX:003524) mice were provided by Jan Breslow, and *LXR* $\alpha^{-/-}$ (JAX stock #013763, RRID: IMSR_JAX:013763) and $\beta^{-/-}$ (JAX stock #014635, RRID: IMSR_JAX:014635) mice were originally provided by David Mangelsdorf. All drug-formulated diets were prepared by Research Diets. For all tumor growth experiments, cells (suspended in 50ul of PBS) were mixed 1:1 with matrigel (356231, BD Biosciences, Bedford, MA) and subcutaneously injected either unilaterally or bilaterally into the lower flank of 6-8 week old sex matched mice. Upon detection of tumor volumes reaching the size indicated in each figure, mice were randomly assigned to a drug treatment or control. GW3956 was administered through formulated drug chow at 100mg/kg/day. RGX-104 was administered either through formulated drug chow at 100mg/kg/day or 50mg/kg/day or delivered via intraperitoneal injection (80mg/kg/day) in a vehicle suspension consisting of corn oil (Sigma) and ethanol (2.5% by volume) as indicated in each figure. Control cohorts were treated with either normal chow (Purina 5001) or with

vehicle consisting of corn oil and ethanol (2.5% by volume), respectively. Tumor measurements were taken on the days indicted throughout the course of the experiment with calipers. For survival analysis, mice were euthanized when total tumor burden approached IACUC guidelines with a tumor burden exceeding 1,500 mm^3 in volume. For the relevant experiments, anti-PD-1 mAb (clone RMP1-14) or a control isotype-matched antibody (BioXCell Cat# BE0089) was administered at 10mg/kg intraperitoneally on days 3, 6, and 9 post-tumor injection. Gvax was generated as previously described and administered at high frequency (every 3 days) during the experiments as indicated.

Patient Details

In this Phase 1 a/b human study, adult patients over age 18 years were enrolled of both sexes. Six sets of patient data were analyzed, including five women and one man, with an age range from 49-67 years (mean 58; median 59). The study is ongoing with a currently planned sample size of 125-135 patients. The protocol was approved by all site Institutional Review Boards and all patients signed informed consent before any screening procedures were obtained.

METHOD DETAILS

Isolation of tumor-infiltrating immune cells

Upon excision, tumors were finely minced and incubated in HBSS (GIBCO) supplemented with 2% FCS (HBSS-2), Collagenase 8 at 0.05mg/mL (Sigma), 1mM sodium pyruvate (GIBCO), 25mM HEPES (Thermo Fisher), and DNaseI at 10mg/mL (Roche) at 37°C on a shaker at 80RPM for 30 minutes. The mixture was then thoroughly triturated and passed through a 70um filter and neutralized with HBSS-2 to dilute the collagenase. Tumor-infiltrating leukocytes were subsequently purified via density gradient centrifugation using Percoll (GE Healthcare). Briefly, the cells were resuspended in 35% Percoll and then 70% Percoll was added to the bottom of the suspension by a glass Pasteur pipette. The suspension was spun at 2100 RPM for 20 minutes at room temperature with the brake off. After the spin, the pellet of red blood cells was removed, as well as excess percoll/buffer, leaving a purified population of tumor-infiltrating leukocytes at the interface. The isolated leukocytes were washed twice with HBSS-2 prior to staining.

Tumor Flow Cytometry

Cell staining for flow cytometry was performed on ice and protected from light. Cells isolated from tissue were incubated with Fc block (TruStain fcX, anti-mouse CD16/32 Ab, Biolegend) to prevent nonspecific binding. The relevant surface antibodies were diluted in Fc block and allowed to incubate for 20 minutes. Cells were subsequently washed and fixed (Fixation Buffer or Fix/Perm, for intracellular staining, BD Biosciences). For intracellular staining, relevant antibodies, diluted in Perm/Wash Buffer (BD Biosciences), were applied to cells and allowed to incubate for 30 minutes. For gp100-tetramer staining, cells were stained with APC-conjugated H-2Db/mGP100 (EGSRNQDWL) tetramer (MBL international Corporation) and antibodies for the other indicated surface markers for 20 min. After staining steps, cells were washed once with FACS buffer (25mM HEPES, 2% FBS, 10mM EDTA, 0.1% sodium azide in PBS) and filtered through 70um mesh prior to flow cytometry analysis. The stained cells were run on a LSRII Flow Cytometer using BD FACSDiva software (BD Biosciences). Data were processed on FlowJo software (Treestar). Forward and side scatter were used to exclude cell debris and doublets.

Isolation of MDSCs

Myeloid-derived suppressor cells were isolated from tissue using the Myeloid-Derived Suppressor Cell Isolation Kit (Miltenyi Biotec) according to the manufacturer's protocol after red blood cell lysis (ACK lysis buffer, Lonza). The purity of the isolated MDSC population was confirmed with flow cytometry to be > 90%.

MDSC *in vitro* Proliferation Assay

Myeloid-derived suppressor cells were isolated as previously described from splenic tissue of tumor-bearing mice. One hundred thousand cells were plated in quadruplicates in poly-L-lysine coated plates. After 3 hours of treatment with 1uM RGX-104 or DMSO as vehicle, cells were fixed with 4% PFA for 15 minutes and wash 3 times with 1X PBS prior staining. Rabbit monoclonal anti-Ki67 antibody (1:400 dilution, Abcam) was applied at 4°C overnight. Cells were incubated with Alexa Fluor 488 secondary antibody (1:200 dilution, Invitrogen) for one hour at room temperature, counterstained with DAPI (1:1000 dilution) and mounted with Prolong Gold (Fisher). For the analysis of the percentage of Ki67 positive cells, five fields from each replicate were imaged at 20x magnification using Zeiss Axio Imager fluorescence microscope. Image analysis was performed using CellProfiler software.

MDSC Adhesion Assay

Myeloid-derived suppressor cells were isolated as previously described from splenic tissue of tumor-bearing mice. One hundred thousand cells were plated in triplicates in poly-L-lysine coated plates. Cells were treated with 1uM RGX-104 or DMSO as vehicle for 2 hours and shaken at 300 rpm for 30 minutes. After this, cells were fixed with 4% PFA for 15 minutes, wash 3 times with 1X PBS, counterstained with DAPI and mounted using Prolong Gold (Fisher). For the analysis, ten fields from each replicate were imaged at 20x magnification using Zeiss Axio Imager fluorescence microscope. The number of remaining cells was determined using CellProfiler software.

In Vitro MDSC Apoptosis Assay

Mouse spleens were isolated from either WT, *LXR*$\alpha\beta^{-/-}$, *Apoe*$^{-/-}$ or *LRP8*$^{-/-}$ mice and homogenized to create a single cell suspension. The cells were treated with 1X ACK Lysing Buffer (10-548E, Lonza) to lyse and remove erythrocytes. MDSCs were isolated from the resulting cell suspension using the Myeloid-Derived Suppressor Cell Isolation Kit (130-094-538, Miltenyi Biotec). Isolated MDSCs were plated onto slides and treated with either RGX-104 or murine recombinant ApoE, at the indicated concentrations and times. The samples were then stained with an antibody against Cleaved Caspase-3 (9661, Cell Signaling).

MDSC mRNA sequencing library preparation

Peripheral blood collected from mice treated with either control or RGX 104 (100 mg/kg) for six days was depleted of erythrocytes through treatment with 1X ACK Lysing Buffer (10-548E, Lonza). MDSCs were isolated using the Myeloid-Derived Suppressor Cell Isolation Kit (130-094-538, Miltenyi Biotec). RNA was extracted from MDSCs using the Total RNA Extraction Kit (17200, Norgen), then purified and concentrated using the RNA Clean & Concentrator −5 Kit (R1016, Zymo Research). The RNA samples were depleted of rRNA using the Ribo-Zero Gold rRNA Removal Kit (MRZG12324, Illumina) then reverse transcribed and prepared for sequencing using the ScriptSeq v2 RNA-Seq Library Preparation Kit (SSV21124, Epicenter).

T Cell *Ex vivo* Suppression Assay

$CD8^+$ T cells were isolated from single cell suspensions of lymph nodes and spleens of naive mice using anti-CD8 microbeads (Miltenyi Biotec) per the manufacturer's protocol. The isolated $CD8^+$ T cells were then labeled with BD Horizon Violet (BV) Proliferation Dye (BD Biosciences) before plating in complete RPMI in round bottom 96-well plates ($5x10^4$ cells/well). Myeloid-derived suppressor cells were isolated from splenic tissue using the Myeloid-Derived Suppressor Cell Isolation Kit (Miltenyi Biotec) according to the manufacturer's protocol after red blood cell lysis (ACK lysis buffer, Lonza). Purified MDSCs were added, in the ratios denoted, to the isolated $CD8^+$ T cells. Subsequently, Mouse T-Activator CD3/CD28 Dynabeads (Thermo Fisher) were added at a bead:T cell ratio of 1:2, and recombinant mouse IL-2 (Invitrogen) at 30U/mL was added and the cultures were incubated for 24 hours at 37C. Control wells were stimulated $CD8^+$ T cells without isolated MDSCs (stim. control), or with MDSC fixed with 100% methanol for 20 minutes at −20°C, or stimulated $CD8^+$ T cells plated with MDSCs isolated from tumor-bearing mice (suppression control). 4.5 hours prior to the end of the 24-hour incubation, Brefeldin A (Sigma) was added to the co-cultures. For testing the direct effect of RGX-104 on T cell activation, the same method was utilized except that no MDSCs were added to the culture.

Isolation of Pmel $CD8^+$ T cells and Adoptive Transfer

$CD8^+$ T cells were isolated from single cell suspensions of lymph nodes and spleens of naive Pmel TCR transgenic mice. A single cell suspension was achieved through grinding the tissue through 70um filters. Following RBC lysis, $CD8^+$ T cells were isolated using anti-CD8 microbeads (Miltenyi Biotec) per the manufacturer's protocol. The $CD8^+$ cells ($2x10^6$) were injected into recipient animals via retro-orbital injection. For gp100 vaccine administration, an emulsion consisting of 25 μg of gp100 peptide (Anaspec) in 15 μL of IFA (Invivogen) was injected into the footpads of mice on the indicated day.

Immunohistochemistry

Immunohistochemistry tissue sections (5um) were generated from frozen tissue prepared in O.C.T. compound (Thermo Fisher) and mounted on Superfrost Plus Microscope Slides (Fisher Scientific). The slides were allowed to thaw at room temperature for one hour prior to staining. The slides were immersed in acetone for 5 minutes at −20°C, followed by 5 minutes in a 1:1 acetone:methanol solution at −20°C, and finally an additional 5 minutes in acetone at −20°C. This was followed by three washes in 1X PBS and 30 minutes of block (5% serum in PBS). Rat anti-mouse Ly6G/Ly6C (Gr-1) (1:1000 dilution, BioXCell) or cleaved caspase-3 (9661, Cell Signaling Technology) was applied at 4°C overnight. Secondary antibodies (1:200 dilution, Invitrogen Alexa Fluor 488 or 594) were added for one hour at room temperature in the dark. DAPI was added (1:1000 dilution) prior to mounting with Prolong Gold (Fisher). For macroscopic lung metastatic nodule visualization, the lungs were extracted and fixed in 4% PFA overnight, paraffin-embedded, sectioned and hematoxylin and eosin stained (Histoserv Inc, Germantown, MD). The slides were imaged on an Olympus IX71 inverted microscope and images were acquired using MetaMorph acquisition software. $CD15^+$ MDSC quantification from paraffin-embedded human tumor biopsies was performed by Cancer Genetics Incorporated (Rutherford, NJ).

In vitro MDSC differentiation assay

MDSCs were generated *in vitro* by co-culture of B16F10 tumor cells with isolated bone marrow cells via the Liechtenstein method. Briefly, 1×10^5 bone marrow cells were isolated from the femurs of mice and cultured in the bottom of 24-well plates in the presence of 1×10^4 B16F10 melanoma cells placed in transwell inserts and grown for 6 days. On day 3, RGX-104 (2uM; dissolved in DMSO vehicle) or DMSO vehicle alone was added to the co-culture. Bone marrow cells cultured alone in the presence of DMSO vehicle (without B16F10 cells or RGX-104 treatment) were run in parallel as a negative MDSC induction control. All cultures were supplemented with 10ng/mL GM-CSF. On day 6, the transwells were removed and cells in the basal chamber were isolated, washed, and then stained for the indicated surface markers for subsequent flow cytometry analysis.

MDSC adoptive transfer

For MDSC adoptive transfer experiments into tumor bearing mice, 2×10^6 MDSCs were isolated as described above from C57BL/6 tumor-bearing mice and subsequently labeled with BD Horizon Violet (BV) Proliferation Dye (BD Biosciences) and then adoptively transferred via retro-orbital injection into wild-type mice. Mice were then treated with RGX-104 (100 mg/kg/day) or control diet for 36 hours. Spleens of recipient mice were then harvested and processed for flow cytometry analysis as described above. For MDSC adoptive transfer experiments in to WT and *Apoe*$^{-/-}$ non-tumor bearing mice, 5×10^6 MDSCs were isolated as described above from tumor-bearing mice (either wild-type C57BL/6 or *Apoe*$^{-/-}$ mice, as indicated in the experiment) and subsequently labeled with BV cell tracker dye and then adoptively transferred via retro-orbital injection into either wild-type or *Apoe*$^{-/-}$ mice as indicated. Mice were then treated with GW3965 (100 mg/kg/day) or control diet for 48 hours. Spleens of recipient mice were then harvested and processed for flow cytometry analysis as described above.

ApoE Protein Production

Murine ApoE (Glu19-Gln311) was cloned into the pGex-6p1 vector (GE Life Sciences) containing an N-terminal GST tag. The protein was overexpressed in *E. coli* BL21 Rosetta (DE3) competent cells (Millipore) induced by 1mM IPTG for 3 hours at 37C in LB medium. Following cell lysis and centrifugation, purified ApoE was achieved by on-column cleavage with PreScission Protease (GE Life Sciences) using glutathione resin-coated columns (GE Life Sciences).

Mouse Genotyping

All mouse genotyping was performed using standard PCR conditions, as recommended by the Jackson laboratory. The genotyping primers used were:

***Apoe*$^{-/-}$ Mice**

Common (Wild-type/Mutant) Forward: 5′-GCC TAG CCG AGG GAG AGC CG-3′
Wild-type Reverse: 5′-TGT GAC TTG GGA GCT CTG CAG C-3′
Mutant Reverse: 5′-GCC GCC CCG ACT GCA TCT-3′

LXR*$\alpha^{-/-}$ *mice

Common (Wild-type/Mutant) Forward: 5′-TCA GTG GAG GGA AGG AAA TG-3′
Wild-type Reverse: 5′-TTC CTG CCC TGG ACA CTT AC-3′
Mutant Reverse: 5′-TTG TGC CCA GTC ATA GCC GAA T-3′

LXR*$\beta^{-/-}$ *mice

Common (Wild-type/Mutant) Forward: 5′-CCT TTT CTC CCT GAC ACC G-3′
Wild-type Reverse: 5′-GCA TCC ATC TGG CAG GTT C-3′
Mutant Reverse: 5′-AGG TGA GAT GAC AGG AGA TC-3′

LRP8*$^{-/-}$ *mice

Mutant Forward: 5′-GAT TGG GAA GAC AAT AGC AGG CAT GC-3′
Mutant Reverse: 5′-GCT TGT TGG AAT TCA GCC AGT TAC C-3′
Wild-Type Forward: 5′-CCA CAG TGT CAC ACA GGT AAT GTG-3′
Wild-Type Reverse: 5′-ACG ATG ACC CCA ATG ACA GCA GCG-3′

Lentiviral shRNA-Based Apoe Gene Knockdown

As previously described (Pencheva et al., 2012), shRNAs were integrated into lentiviral particles that were prepared by transfection of 6 ug of vector A, 12ug of vector K, and 12 ug of shRNA plasmid into HEK293T packaging cells. Subsequent lentiviral shRNA transduction was conducted in the presence of 10 ug/ml of polybrene (for 6 hr). The cells were then expanded for 72 hr after transduction, and lentiviral selection was performed by culturing cells in the presence of 2 ug/ml of puromycin (P8833, Sigma-Aldrich) for 72 hr. The following shRNA sequence was used:

5′-CCGGGAGGACACTATGACGGAAGTACTCGAGTACTTCCGTCATAGTGTCCTCTTTTT-3′

Human MDSC and T cell Flow Cytometry Analysis

Blood samples were obtained from either healthy volunteers or patients with cancer enrolled in the RGX-104 clinical trial. For samples from RGX-104 trial patients, peripheral blood was obtained at weekly intervals by health-care providers at the indicated times in the figure. Week 0 corresponds to a pre-treatment sample obtained immediately prior to receiving the first dose of RGX-104. To avoid degradation of samples and ensure stable MDSC populations for quantification, blood samples were drawn into Cyto-Chex tubes (un-frozen) and analyzed within 24 hours of collection from patients and run as two technical replicates for flow cytometry analysis. Flow cytometry analysis of human blood samples was performed by Serametrix Corporation (Carlsbad, California). After processing,

the cells were stained with the indicated surface antibodies and subsequently run on a LSRII Flow Cytometer using BD FACSDiva software (BD Biosciences). Data were processed on FlowJo software (Treestar). MDSC quantification analysis of samples was conducted on total cells remaining after dead cells, doublets, and SSC^{high} neutrophils were excluded using forward and side scatter. To ensure consistent gating of MDSCs and activated CTLs, control samples were run with each patient sample to define appropriate gating boundaries for relevant markers (e.g., HLA-DR negative control to determine expression cut-off for MDSCs gating). Across a sample set of blood analyzed from patients with cancer and healthy volunteers, greater than 98% of $CD15^{+}CD33^{+}HLA\text{-}DR^{low}$ G-MDSCs also expressed the G-MDSC marker CD11b (Figure S6A). Therefore, staining for CD11b was not included in subsequent analysis of patient samples from the RGX-104 clinical trial.

Clinical Study Design

This Phase 1 a/b study is open-label, multi-center and single-arm, whose primary objective is to determine the maximum-tolerated dose, or maximum tested dose at which multiple dose-limiting toxicities (DLTs) are not observed, of RGX-104. Inclusion and exclusion criteria are stipulated, requiring all patients to have a pathologic confirmation of a locally advanced or metastatic solid tumor or lymphoma that has been deemed refractory to standard therapies. Patients may not have any other active malignancy that could confound the study endpoints. Patients must not have a history of pancreatitis, active Hepatitis B or C, or any illness/social situation in the opinion of the treating investigator that would limit compliance with the study requirements. Patients are not allowed to be treated with any other anti-neoplastic therapies while on study nor to have received any prior treatment with an LXR agonist. Typical Phase 1 study parameters are required for performance status, hematologic and other organ function measurements. Patients are required to use acceptable contraceptive methods while on study and for a specified time period thereafter. Concomitant medications are restricted only if they pose a clinical risk of drug-drug interactions. Treatment for any condition with corticosteroids is not allowed unless at doses less than 10 mg daily prednisone equivalents. Patients were treated with RGX-104 at 120 mg QD or 240 mg QD for three weeks, according to the patient cohort to which they were enrolled, followed by a one-week break. Patients continued treatment with RGX-104 until treatment intolerance or progression of disease. The primary endpoint is incidence of DLTs, which are evaluated by the Rgenix sponsor medical monitor in collaboration with all treating clinical investigators. Secondary endpoints include pharmacokinetic measurements of RGX-104 and its metabolites in plasma and urine. Exploratory endpoints include the following: expression of Apolipoprotein E (ApoE) and ApoE receptor in tumor specimens prior to, during, and post-treatment; ApoE gene-expression in whole blood prior to, during, and post-treatment; quantitative and qualitative effects of RGX-104 on various immunologic effector cells, including Myeloid Derived Suppressor Cells (MDSCs) and T cells. Ultimately, efficacy endpoints will be obtained on a large sample size of patients in disease-specific expansion cohorts. Dose-limiting toxicities are defined as any of the following toxicities occurring during the first 4 weeks of treatment that are not clearly related to another cause (i.e., disease progression): any grade $\geq$ 3 non-hematologic AE, with the exceptions of Grade 3 nausea, vomiting, diarrhea, constipation, fever, fatigue, or skin rash in which there has been suboptimal prophylaxis and management that resolves to Grade $\leq$ 2 within 72 hours; grade 4 thrombocytopenia, or Grade 3 thrombocytopenia with Grade > 1 bleeding or requirement for platelet transfusion; grade 4 neutropenia; grade $\geq$ 3 febrile neutropenia; grade $\geq$ 3 transaminase (AST/ALT) elevation; any toxicity resulting in > 25% held/skipped doses during the cycle; any other significant toxicity considered by the Investigator and Sponsor's medical representatives to be dose-limiting.

Clinical Assessments

Adverse events were collected from the time the patient signed Informed Consent and were graded using Common Terminology Criteria for Adverse Events version 4.03. Tumor response was evaluated per Immune-Related Response Criteria or International Working Group criteria for malignant lymphoma. Tumor assessments were performed at screening, at approximately 8 weeks after starting RGX-104, or sooner if clinical signs and symptoms warranted. Radiographic imaging for assessment of tumor lesions was performed using computed tomography, positron emission tomography, magnetic resonance imaging, or ultrasound. Clinical measurements of palpable tumor lesions were conducted with calipers. Assessment of progression of disease was to be confirmed by assessment of measurable index lesions and any new measurable lesions 4 weeks later. Patients who were clinically stable were permitted to continue treatment pending confirmation of disease progression.

QUANTIFICATION AND STATISTICAL ANALYSIS

Data Analysis

Significance of tumor growth curve comparisons was carried out using unpaired t tests. The Mantel-Cox log-rank test was used for statistical comparisons in survival analyses. Statistical comparisons of pre-treatment and post-treatment MDSC levels from human patients were carried out using a paired t test. Statistical comparisons of proliferation and adhesion upon LXR agonism were carried out using Student's t test. All other statistical comparisons were carried out using the non-parametric Mann-Whitney test. CellProfiler analysis software was used to quantify nuclear staining, as well as the markers cleaved caspase-3 and Ki67. Throughout all figures: $^{*}p < 0.05$, $^{**}p < 0.01$, and $^{***}p < 0.001$, $^{****}p < 0.0001$. Significance was concluded at $p < 0.05$.

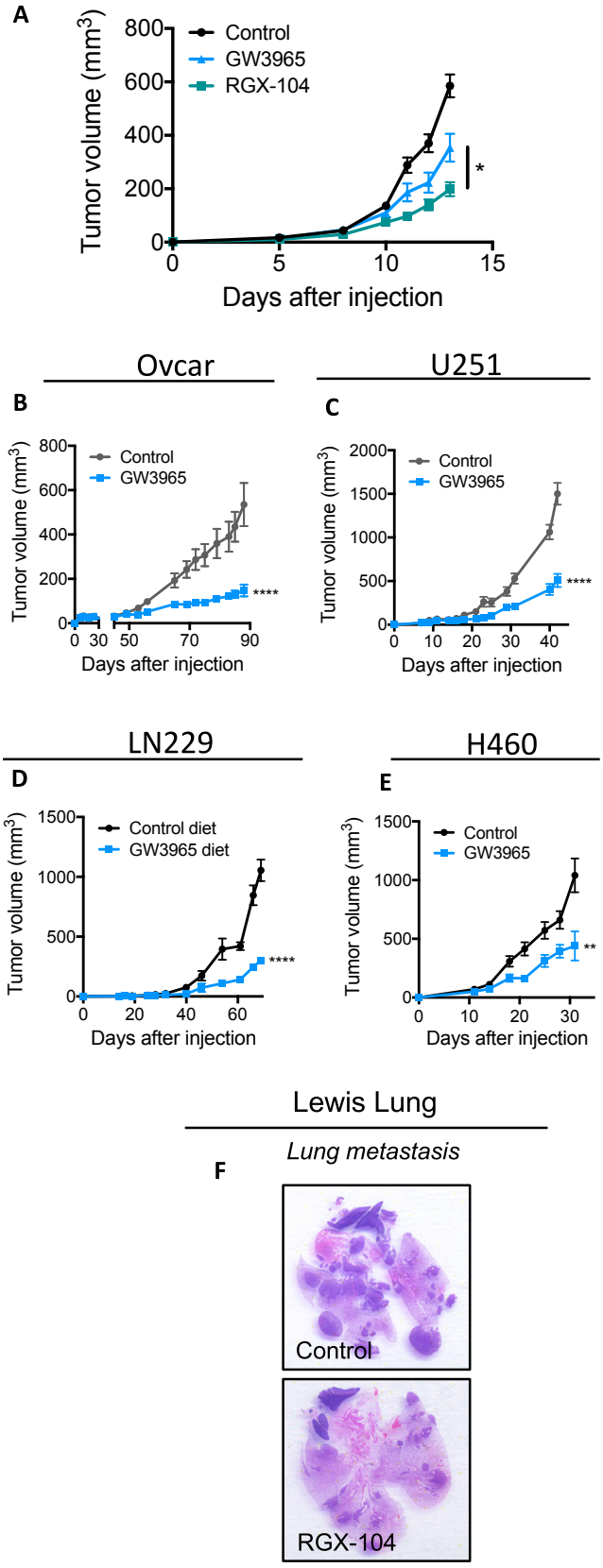

(legend on next page)

Figure S1. Treatment with LXR Agonists Suppresses Tumor Growth and Metastasis in Diverse Cancer Types, Related to Figure 1

(A) Tumor growth by 5×10^4 B16F10 cancer cells subcutaneously injected into C57BL/6 mice. Following tumor growth to 5-10 mm^3 in volume, mice were fed either control chow, chow supplemented with GW3965 (100 mg/kg), or chow supplemented with RGX-104 (100 mg/kg) ($n \geq 6$).

(B–E) Tumor growth by 5×10^6 OVCAR ovarian cancer cells (B), 5×10^6 U251 glioblastoma cells (C), 1×10^6 LN229 glioblastoma cells (D), and 1×10^6 H460 lung cancer cells (E) subcutaneously injected into NOD SCID mice. Following tumor growth to 5–10 mm^3 in volume, mice were fed a control chow or a chow supplemented with GW3965 (100 mg/kg) until termination of the experiment at the indicated days ($n \geq 5$).

(F) Macroscopic lung nodules in H&E-stained lungs extracted 15 days after subcutaneous injection of 5×10^4 LLC lung cancer cells; mice were fed a control chow or a chow supplemented with RGX-104 (100 mg/kg) for ten days starting when tumors were 30-40 mm^3 (from Figure 1I).

Data represent mean ± s.e.m.

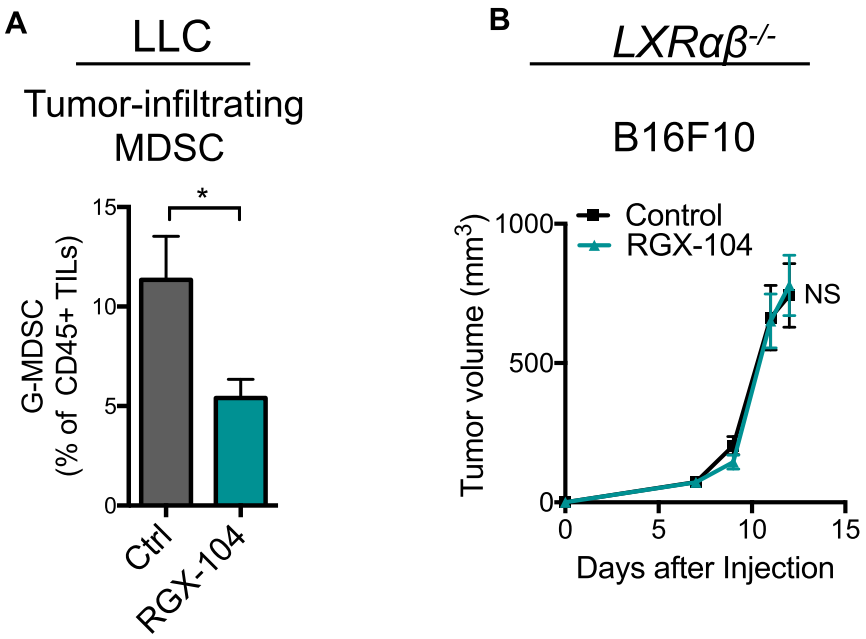

Figure S2. LXR Agonists Deplete CD11b^{+}Gr-1^{+} MDSCs, Related to Figure 2

(A) Percent tumor-infiltrating total G-MDSCs of total CD45^{+} TILs in LLC tumors in mice treated with control or RGX-104 (100 mg/kg) (n = 7).

(B) Tumor growth by 5 × 10^{4} B16F10 cancer cells grown in *LXRαβ* $^{-/-}$ mice treated with control or RGX-104 (100 mg/kg) when tumors reached 5-10 mm^{3} (n ≥ 6).

Data represent mean ± s.e.m.

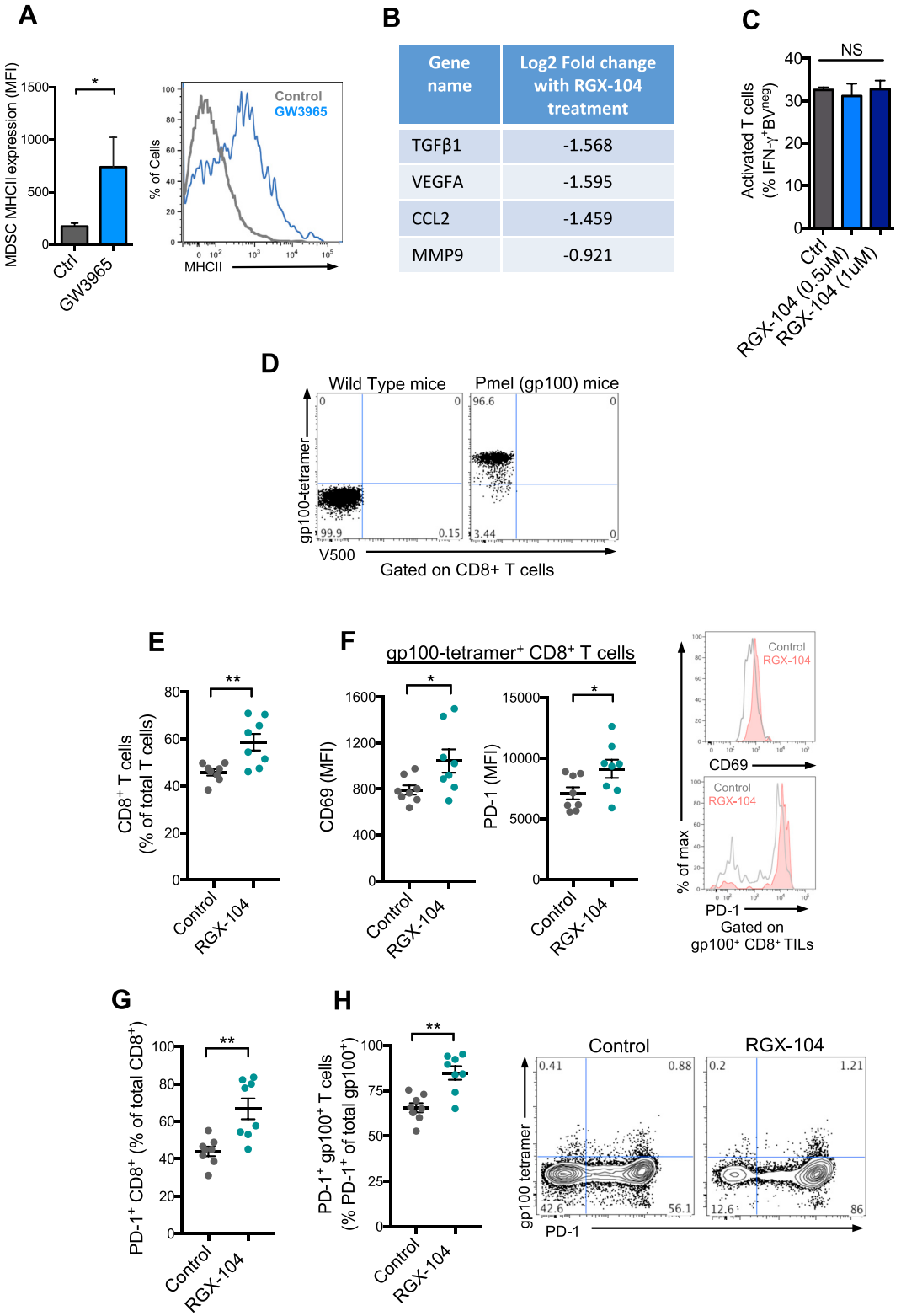

Figure S3. LXR Agonism Induces a More Mature Phenotype for CD11b$^+$ Gr-1$^+$ Tumor-Infiltrating MDSCs, Related to Figure 3

(A) Mean fluorescent intensity (MFI) of MHC-II expression on G-MDSCs in B16F10 tumors from mice treated with control or GW3965 (100 mg/kg) for 10 days ($n \geq 4$). Representative histogram plot of MHC-II expression on tumor G-MDSCs in control and GW3965 treated mice.

(legend continued on next page)

(B) Gene expression values (Log2FC) for established MDSC effector genes detected by mRNaseq analysis of MDSCs obtained from *in vivo* RGX-104 treated animals (n = 3) or control animals (n = 3). Fold change values reveal downregulations in expression of MDSC effector genes upon LXR agonism.
(C) Percent activated $CD8^+$ T cells as assessed by IFN-γ expression and dilution of proliferation dye (BV) in the presence of DMSO (control) or RGX-104 (in DMSO) at the indicated concentrations for 24 hours *in vitro* (n = 4).
(D) As a positive control to establish gating for gp100 antigen-specific T cells, B16F10 tumors were implanted into either wild-type mice or Pmel transgenic mice that solely generate T cells with gp100-specific T cell receptors. Contour plots show the population of gp100-antigen specific (gp100-tetramer$^+$) $CD8^+$ T cells from either wild-type mice (left) or Pmel transgenic mice (right) in the absence of LXR agonist treatment.
(E) Percent $CD8^+$ T cells of total tumor-infiltrating TCR$\alpha\beta^+$ T cells from B16F10 tumors of control or RGX-104-treated wild-type mice (100 mg/kg; 8 days) (n = 8).
(F) Mean fluorescent intensity (MFI) of CD69 expression (left) and PD-1 expression (right) on tumor-infiltrating gp100-tetramer$^+$ $CD8^+$ T cells in B16F10 tumors from wild-type mice treated with control or RGX-104 (100 mg/kg) for 8 days (n = 8). Representative histogram plots show CD69 and PD-1 expression on tumor-infiltrating $gp100^+$ $CD8^+$ T cells from control and RGX-104 treated mice.
(G) Percent PD-1^+ $CD8^+$ T cells of total tumor-infiltrating $CD8^+$ T cells from B16F10 tumors of control or RGX-104-treated wild-type mice (100 mg/kg; 8 days) (n = 8).
(H) Percent PD-1^+ gp100-tetramer$^+$ $CD8^+$ T cells of total tumor-infiltrating gp100-tetramer$^+$ $CD8^+$ T cells from B16F10 tumors of control or RGX-104-treated wild-type mice (100 mg/kg; 8 days) (n = 8). Representative flow plots show expression of gp100-tetramer and PD-1 on tumor-infiltrating $CD8^+$ T cells from control and RGX-104 treated mice.

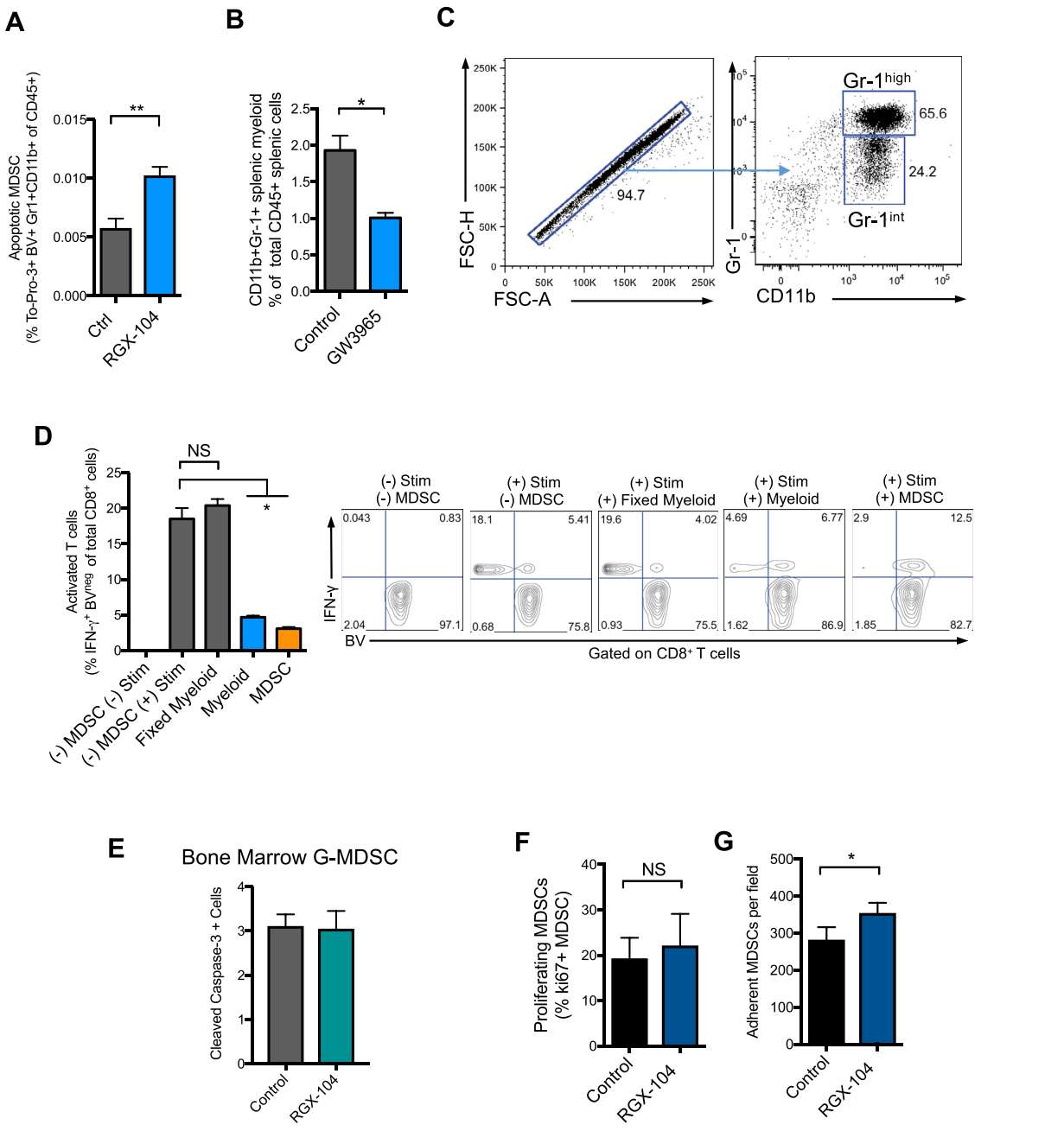

Figure S4. LXR Agonism Regulates MDSC Survival, Related to Figure 4

(A) Percentage of To-Pro-3$^+$ labeled adoptively transferred MDSCs of total CD45$^+$ splenocytes from tumor-bearing recipient mice treated for 36 hours with RGX-104 (100 mg/kg) or control after adoptive transfer (n = 8).

(B) Percentage of CD11b$^+$Gr-1$^+$ myeloid cells of total CD45$^+$ splenocytes in non-tumor-bearing mice treated for 48 hours with GW3965 (100 mg/kg) or control ($n \geq 5$).

(C) Representative plots showing the relative proportion and purity of granulocytic (CD11b$^+$Gr-1^{high}) and monocytic (CD11b$^+$Gr-1^{int}) myeloid cells recovered after affinity purification from the spleen using MACs MDSC isolation kit.

(D) Suppressive properties of CD11b$^+$Gr-1$^+$ myeloid cells isolated from spleens of mice as assessed by CD8$^+$ T cell activation (IFN-γ expression) and proliferation (BV dilution) after 24-hour co-culture. Representative contour plots show IFN-γ expression and BV fluorescence of CD8$^+$ T cells. Fixed myeloid cells were pre-treated with methanol to neutralize activity of any immunosuppressive signals while maintaining any physical effects that could alter T cell activation as an additional control (n = 4).

(E) Percentage of cleaved Caspase-3$^+$ CD11b$^+$Ly6G$^+$ G-MDSCs isolated from bone marrow of B16F10 tumor bearing mice as a percentage of total CD11b$^+$Ly6G$^+$ G-MDSCs, after *in vitro* treatment with RGX-104 (1uM) or vehicle control for 3 hours (n = 7).

(legend continued on next page)

(F) Quantification of the percentage of proliferating MDSCs identified as Ki-67 positive cells in control and RGX-104 treated MDSCs isolated from tumor bearing mice (n = 3).
(G) Number of total adherent MDSCs (per field) purified from tumor bearing mice after treatment with RGX-104 for 2 hours (n = 3).
Data represent mean ± s.e.m.

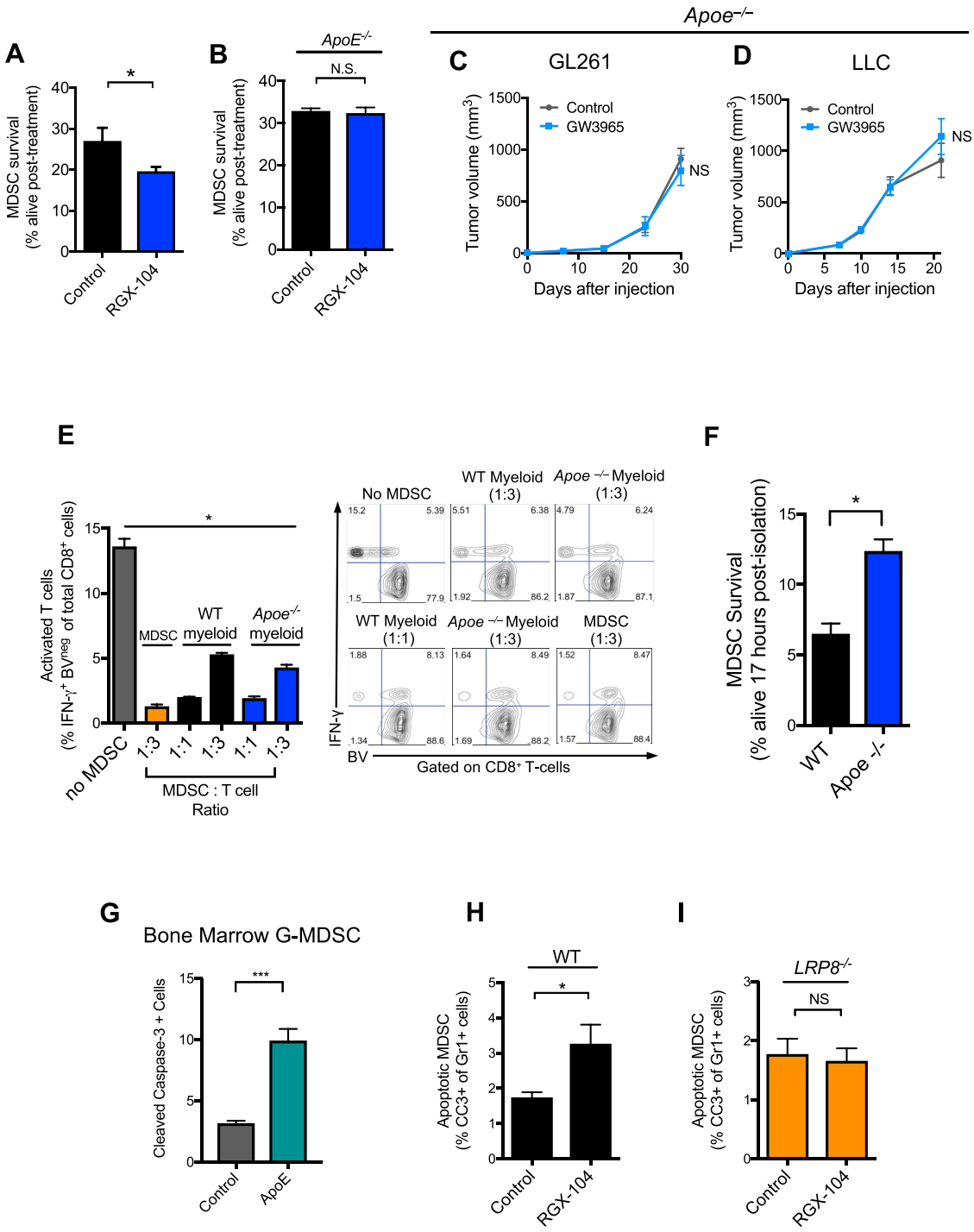

Figure S5. ApoE Is Required for the Anti-tumor Activity of LXR Agonists, Related to Figure 5

(A) *In vitro* survival assay of splenic MDSCs harvested from C57BL/6 WT mice, treated with or without 0.5μM RGX-104. Data reported as percentage of surviving cells as assessed by trypan blue staining (n = 4).

(B) *In vitro* survival assay of splenic MDSCs harvested from *Apoe* −/− mice, treated with or without 0.5μM RGX-104. Data reported as percentage of surviving cells as assessed by trypan blue staining (n = 4).

(C and D) Mean tumor growth of control or GW3956 treated (100 mg/kg) ApoE-depleted (shRNA) GL261 (C) or ApoE-depleted (shRNA) LLC (D) tumors injected into *Apoe* $^{-/-}$ mice. Treatment was started when tumors reached 5–10 mm^3 in volume and continued until termination of the experiment at day 30 (C) and 21 (D) (n = 5).

(legend continued on next page)

(E) Suppressive properties of myeloid cells isolated from WT and *Apoe*$^{-/-}$ mice as assessed by CD8$^+$ T cell activation (IFN-γ expression) and proliferation (BV dilution) after 24 hour co-culture at the designated myeloid cell:T cell ratio. Representative contour plots show IFN-γ expression and BV fluorescence of CD8$^+$ T cells (n = 4).

(F) *In vitro* survival assay of splenic MDSCs harvested from C57BL/6 WT or *Apoe* −/− mice cultured for 17 hours. Data reported as percentage of surviving cells as assessed by trypan blue staining (n = 4).

(G) Percentage of cleaved Caspase-3$^+$ CD11b$^+$Ly6G$^+$ G-MDSCs isolated from bone marrow of B16F10 tumor bearing mice as percentage of total CD11b$^+$Ly6G$^+$ G-MDSCs, after *in vitro* treatment with rmApoE or vehicle control for 3 hours (n = 7).

(H) Percent cleaved caspase-3$^+$ (CC3+) Gr1$^+$ MDSCs in the spleen of wild-type (WT) B16F10-tumor bearing mice treated *in vivo* with RGX-104 (100 mg/kg) or control. 5 sections per spleen were imaged to calculate an average number of double positive cells per high-power field (n = 5).

(I) Percent cleaved caspase-3$^+$ (CC3+) Gr1$^+$ MDSCs in the spleens of *LRP8*$^{-/-}$ B16F10-tumor bearing mice treated *in vivo* with RGX-104 (100 mg/kg) or control. 5 sections per spleen were imaged to calculate an average number of double-positive cells per high-power field (n = 5).

Data represent mean ± s.e.m.

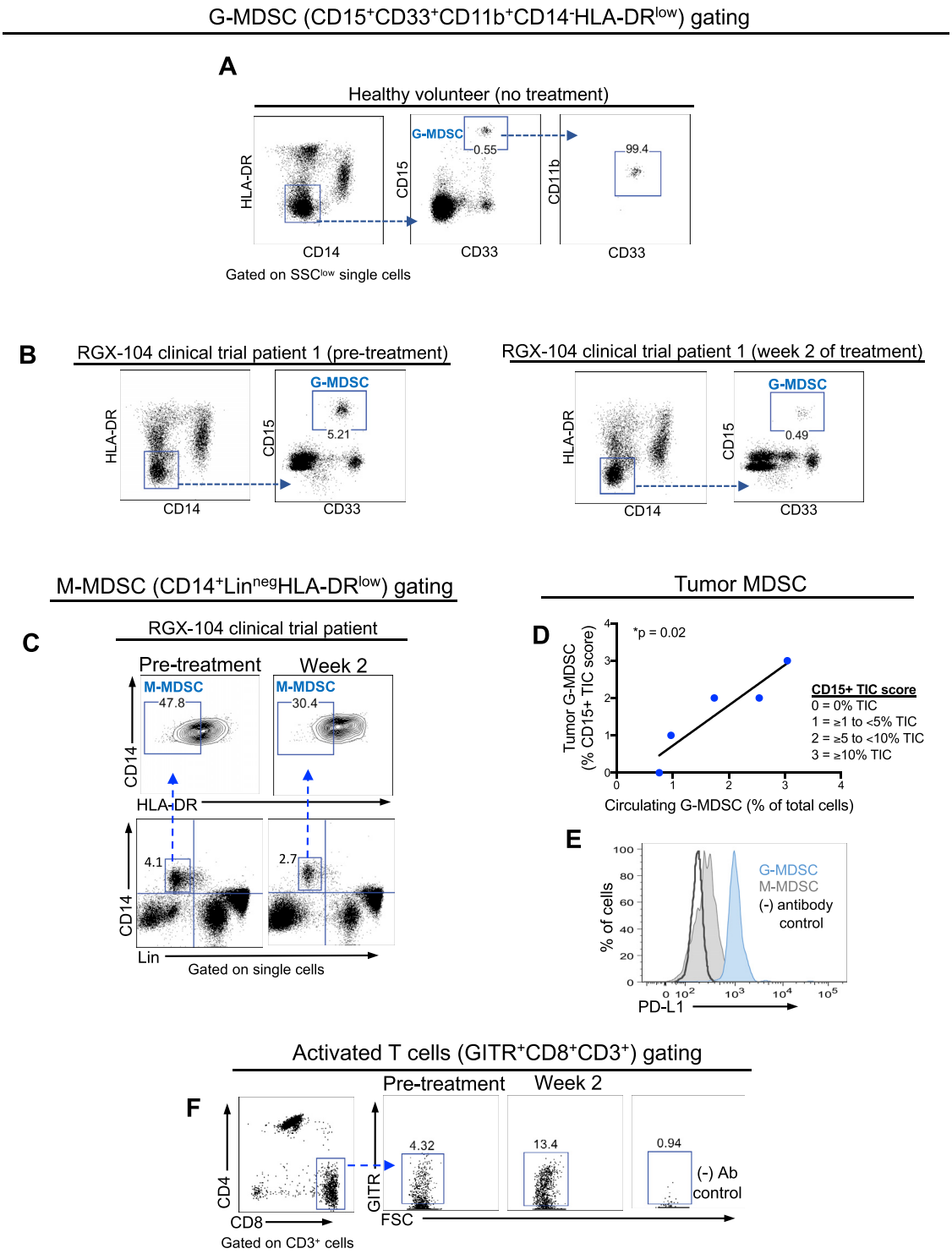

Figure S6. Gating Strategy for Characterizing MDSC and T Cell Populations, Related to Figure 7

(A) Gating strategy for circulating G-MDSCs is shown in a representative healthy volunteer.

(B) Using the gating scheme in (A), representative flow plots showing the G-MDSC population in a cancer patient treated with RGX-104, comparing pre-treatment with week 2 after treatment initiation.

(C) Gating strategy for identifying circulating M-MDSCs is shown for a representative cancer patient treated with RGX-104, comparing pre-treatment and week 2.

(legend continued on next page)

(D) Correlation between pre-treatment levels of circulating G-MDSCs and tumor-infiltrating G-MDSCs from available paired biopsies in patients prior to being treated with RGX-104. Tumor G-MDSCs were quantified as a score based on the percentage of tumor-infiltrating cells (TIC) that were $CD15^{+}$ in the ranges indicated in the figure (n = 5).

(E) Representative histogram plot comparing PD-L1 expression on G-MDSCs and M-MDSCs from a cancer patient prior to treatment with RGX-104.

(F) Gating strategy for activated ($GITR^{+}CD8^{+}$) T cells in a representative cancer patient treated with RGX-104, comparing pre-treatment with week 2 after treatment initiation.